東京大学 大学院新領域創成科学研究科

基盤科学研究系

先端エネルギー工学専攻

平成 23 年度

修士論文

An ECH Dipole Plasma Device for Examining
the Weakly-Ionized Regime

弱電離状態の検討のための ECH 磁気圏型プラズマ装置

47096127　Germán Vogel

Contents

To God,
to all those suffering
in the world
for the oblivion
in Him.

Chapter 1

Introduction

The present work describes the planning, implementation and first approaches at diagnostics of a new experimental device for the confinement of ECH plasma in a magnetosphere-like configuration aimed at the study of the weakly-ionized regime, in which energy transport mechanisms of second order in the MHD domain become significant in Hall MHD [7][8]. Exploring these phenomena can yield for applications in astronomical plasmas such as the solar corona as well as deepening the understanding of nuclear fusion transport processes [12][14][17][18].

1.1 Framework on Dipole Confinement

Based on the observations of the Jovian magnetosphere in 1987, Akira Hasegawa at AT&T Bell Laboratories postulated [1] that a magnetic dipole configuration could improve the conditions of hot plasma confinement for nuclear fusion applications, with the possibility of boosting the plasma's beta, and making it immune to anomalous transport.

In parallel, Mahajan and Yoshida have developed a magnetofluid model based on a double curl Beltrami flow and Taylor relaxation states, under which they observed [2] the significance of the $\nabla \times \boldsymbol{B} \sim \boldsymbol{J}$ term in the induction equation, the responsible for the rise of

diamagnetic structures, which accentuates similar possible benefits offered by the magnetospheric plasma configuration with regards to higher beta and stability. Their approach on including a larger set of equations coupling the magnetic and the fluid aspects of plasma yields structures that are richer than those in a Beltrami-Taylor system, which comes about from exploring the simplest equilibrium solution to generalized vortices equations leading to,

$$\boldsymbol{B} = a\left(\boldsymbol{V} - \nabla \times \boldsymbol{B}\right) \tag{1}$$

$$\boldsymbol{B} + \nabla \times \boldsymbol{V} = b\,\boldsymbol{V} \tag{2}$$

where new physical phenomena are expected to come about. Due to the fact that one here deals with lowest free energy states, the same MHD stability which Hasegawa found promising in a planetary magnetosphere such as the one of Jupiter, is naturally expected.

1.2 Dipole Confinement Characteristics and Advantages

Three periods are present in a dipole magnetic field which make it possible for motion to become integrable and help understand the single-particle trajectories in such a configuration: the gyro motion that a charged particle describes around the magnetic field lines, the bounce motion which is instead along the magnetic field, and the drift motion in the toroidal direction.

The pressure profiles needed for dipole confinement to be generated near marginal stability towards immunity to fluctuations of magnetic and electric nature, were found [3] by Hasegawa to scale like $r^{-20/3}$, at which the big burden of neo-classical confinement losses in tokamaks are spared. Aside from this, one characteristic aspect of dipole plasma is the radius of curvature being smaller than the pressure scale length. Such good energy confinement and high beta capabilities are of utmost need for second generation nuclear fusion reactors which can burn advanced fuels and provide for more flexibility on that regard than tokamaks. Not to mention that steady state operation is theoretically possible in the dipole approach, whereas it is tightly off boundaries for the magnetically toroidal devices.

The need for pressures that scale like $p \sim r^{-20/3}$ comes from the need for an adiabatic variation of the plasma pressure, $p \sim V^{-5/3}$, so that a spatial pressure variation will be stable with respect to MHD instabilities. Under such consideration, the plasma will be confined steadily even if curvature is overall bad [4].

Perhaps one of the facts with the strongest consequences in drawing a contrast between what we could call first (tokamaks) and second (dipole confinement) generation approaches at nuclear fusion, lies in their geometry, for in the first the plasma is confined within the sources of the magnetic field – that is, the toroidal coils –, whereas a dipole, naturally confines plasma on the outside of the field source. This alone results in an increased flexibility not only of operation, but is one of the key factors at allowing for a hot plasma that is free of disruptions.

Disruptions such as ballooning and interchange modes present in high beta plasma are precisely avoided due to the fact that the plasma profiles in a dipole device present gradients that are smooth enough. What we are to win from it is to eventually be able to bypass the problem of a tritium breeding blanket – a big technical burden in the commercial tokamak reactors being developed and implemented nowadays – that is no longer necessary upon burning advanced fuels such as D^3He and DD.

Another benefit of dipole confinement plasma devices is its inherently steady state operation, not requiring of current-drive methods or workarounds for it, which has occupied to a big extent the efforts in the research of nuclear fusion scientists and engineers.

One of the demerits of dipole confinement is the need of levitating the source of the magnetic field – a current ring – which also needs to operate under persistent current mode in order to avoid contact losses in the supporting structures. This is a significant technical problem, which has however been satisfactorily been addressed in the implementations of big projects on dipole confinement such as the ones mentioned in the following passages. The need for levitation still acts as an operation time constraint, as a persistent current needs of proper cooling for maintaining superconducting qualities, and these can't be maintained without supporting structures.

1.3 Dipole Confinement Implementation

Along the lines of tapping the above-mentioned benefits, the theoretical approach of Hasegawa has materialized in the implementation of the Levitated Dipole eXperiment (LDX) device in a joint project between MIT and Columbia University under the lead of professors Kesner and Mauel. Whereas the new models of Yoshida and Mahajan have been implemented in the Ring-Trap project in the University of Tokyo under the lead of professor Yoshida [20] [21][22][23].

In the latter case, the Mini-RT project succeeded [5] to demonstrate the the plasma production with 2.45 GHz and 2.8 kW microwave power, noting that the levitation of the internal coil serving as dipole field source is key at improving the plasma parameters dramatically, enabling operation at lower filling pressures. The order of electron densities obtained in such experiments has been above $10^{17} m^{-3}$. It was built under the parameters of $R = 0.15\text{m}, I_c = 50\text{kAturns}$, and persistent current switch for an HTS coil was needed as described above.

The RT-1 device also using 2.45 GHz electron-cyclotron heating has demonstrated long confinement times for almost pure electron plasmas, of above 0.1 s and high beta plasma generation towards unity [6]. In both cases the launching of ECH waves in the equatorial plane acts as the main mechanisms for the generation of plasma, when the frequency of the waves is set to match the cyclotron frequency for 0.0875 T. Its operation time is limited to 6.5 hours due to the decay of current in the levitated coil which is cooled at 20 K and operated until reaching 40 K. The position of the coil was measured with laser detectors, and levitation coil is controlled with PD feedback system. The coil current was directly charged by power supply through removable current feed-through. All of these considerations give an idea of the technical burdens that rise on the need for the levitation of the superconducting magnetic that acts as the field source for confining a dipole plasma.

Experimentation is recent as RT-1 obtained plasma for the first time in 2006 [24][25][26], and research is ongoing towards the direct heating of ions – that is, not just through mode conversion of the ECH waves injected. Such ongoing research plasma is produced and

confined at outer region of the torus region – limited between the chamber walls and the central coil –, where interchange mode might be unstable. The purposes are to study relaxation physics in fusion plasma, high beta configurations.

1.4 The Low-Ionized Plasma Regime

The study of plasma in the low-ionized regime is interesting because it presents possible applications both in the fields of nuclear fusion – whereas in aiming for a more complete physical description of ion dynamics in fusion plasmas as well as in addressing plasma regions such as the divertor in a tokamak where neutral components begin to present significance –, as well as in the field of astronomical plasmas and the trending topic of space weather, which requires for an understanding of plasma physics both at the solar corona region, as well as of interstellar plasma and the own Earth's magnetosphere. In the latter case, space weather scientists have relied on numeral simulations, with more direct and realistic measurements of the Earth magnetosphere to be kick started in the coming years by NASA. Linear and non-linear free-force magnetic configurations and non-linear Beltrami flow field are general features of astrophysical plasmas (Keplerian rotation involved).

Krishan and Yoshida [7] developed a useful formalism for a description of the energy dissipation mechanisms that operate in a weakly-ionized plasma regime, where the behavior of neutral and ion dynamics can no longer be neglected.

The non-ideal effects that are involved in a weakly-ionized plasma are Hall effect and ambipolar diffusion. These are important contributors and work for different density regimes. They are directly derived from the equations of motion of the three fluid components involved.

Firstly, the equation of motion for electrons – via Navier-Stokes –,

$$m_e n_e \left[\frac{\partial \vec{V}}{\partial t} + \left(\vec{V}_e \cdot \vec{\nabla} \right) \vec{V}_e \right] = -\vec{\nabla} p_e - e n_e \left[\vec{E} + \frac{\vec{V}_e \times \vec{B}}{c} \right] - \nu_{en} \rho_e \left(\vec{V}_e - \vec{V}_n \right) \qquad (3)$$

gives the electric field in an intertialess case justified as an Ohm's law,

$$\vec{E} = -\frac{\vec{V}_e \times \vec{B}}{c} - \frac{\vec{\nabla} p_e}{e\, n_e} - \frac{\nu_{en}\left(\vec{V}_e - \vec{V}_n\right)}{e\, n_e} \tag{4}$$

Due to the fact that the ionization ratio $\alpha = \rho_i / \rho_n \ll 1$, the ion dynamics can be neglected, as long as the electron-neutral collision frequency is larger than ion-collision frequency. Thus, the ion force balance can be written,

$$0 = -\vec{\nabla} p_i + e\, n_i \left[\vec{E} + \frac{\vec{V}_i \times \vec{B}}{c} \right] - \nu_{in} \rho_i \left(\vec{V}_i - \vec{V}_n \right) \tag{5}$$

Again, once more the low ionized approximation and the fact that ni / ne=1, the relative neutral-ion velocity can be expressed,

$$\vec{V}_n - \vec{V}_i = \frac{\nabla (p_i + p_e)}{\nu_{in} \rho_i} - \frac{\vec{J} \times \vec{B}}{c\, \nu_{in} \rho_i} \tag{6}$$

where J,

$$\vec{J} = -e\, n_e \left(\vec{V}_e - \vec{V}_i \right) \tag{7}$$

Finally, the neutral fluid motion equation,

$$\rho_n \left[\frac{\partial \vec{V}_n}{\partial t} + \left(\vec{V}_n \cdot \vec{\nabla} \right) \vec{V}_n \right] = -\vec{\nabla} p_n - \nu_{ni} \rho_n \left(\vec{V}_n - \vec{V}_i \right) - \rho_n \vec{\nabla} \phi_g + \mu \nabla^2 \vec{V}_n \tag{8}$$

and the consideration over the collision frequencies $\nu_{in}\rho_i = \nu_{ni}\rho_n$ allows us to deduce that neutrals are seen as affected by Lorentz force. This daunting result comes from the strong ion-neutral coupling precisely due to the collisions.

$$\rho_n \left[\frac{\partial \vec{V}_n}{\partial t} + \left(\vec{V}_n \cdot \vec{\nabla} \right) \vec{V}_n \right] = -\nabla p + \frac{\vec{J} \times \vec{B}}{c} - \rho_n \vec{\nabla} \phi + \mu \nabla^2 \vec{V}_n \tag{9}$$

The unique terms that become significant in Hall MHD, that is, the Hall term $\vec{J}/e\,n_e$ and ambipolar diffusion $\vec{J} \times \vec{B}$ terms, now extracted from Faraday law of induction,

$$\vec{\nabla} \times \vec{E} = -\frac{\partial \vec{B}}{\partial t} \tag{10}$$

using the electric field E from (4) from the electrons' equation of motion, and the relative velocities of (6),

$$\frac{\partial \vec{B}}{\partial t} = \vec{\nabla} \times \left[\left(\vec{V}_n - \frac{\vec{J}}{e\,n_e} + \frac{\vec{J} \times \vec{B}}{c\,\nu_{in}\rho_i} - \frac{\vec{\nabla}\left(p_e + p_i\right)}{\nu_{in}\rho_i} \right) \times \vec{B} \right] + \eta \nabla^2 \vec{B} \tag{11}$$

where $\eta = m_e \nu_{en} c^2 / 4\pi e^2 n_e$ is the electrical resistivity due to electron-neutral collisions. There will be then two cases when the Hall term is much bigger than the ambipolar diffusion term: 1) under a large density of neutral particles, 2) due to $\nu_{in} \gg \omega_{ci}$.

Because of the variety of ionization processes that affect the ionization ratio, which make an estimation of it difficult, it is common to relate it to the temperature through Saha's ionization equation as an effective equivalent temperature,

$$\frac{n_i}{n_n} = \frac{2 Z_{ionized}}{n\,Z_{ground}} \left(\frac{2\pi\,m_e\,k\,T_e}{h^2} \right)^{3/2} e^{-X/kT_e} \tag{12}$$

Here, $Z_{ionized}$ / Z_{ground} are the weighted averages of fraction of neutral atoms in each energy state, h is Planck's constant, and X is the energy to ionize an atom from the ground state.

We see then that in a weakly ionized plasma, the description of the evolution of magnetic field by a generalized Ohm's law includes the Hall effect and ambipolar diffusion terms. Turbulence, viscosity, resistivity, and ambipolar dissipation mechanisms rise as a product of the extra spatial and temporal scales that are introduced by this.

The mechanism of energy dissipation that the system chooses will depend on the properties of the plasma and the energy injection rate. Krishan and Yoshida have shown [8] that for the partially ionized solar atmosphere, the ambipolar diffusion mechanism dominates for a large energy injection rate.

The equations that describe dynamics of weakly ionized plasma,

$$\frac{\partial \vec{V}}{\partial t} + \left(\vec{V} \cdot \vec{\nabla} \right) \vec{V} = -\nabla h + \frac{\vec{J} \times \vec{B}}{c \, \rho_n} + \mu \nabla^2 \vec{V} \tag{13}$$

and,

$$\frac{\partial \vec{B}}{\partial t} = \vec{\nabla} \times \left\{ \left[\vec{V} - \frac{\vec{J}}{e \, n_e} + \frac{\vec{J} \times \vec{B}}{c \, \nu_{in} \rho_n} \right] \times \vec{B} \right\} + \eta \nabla^2 \vec{B} \tag{14}$$

can be expressed in dimensionless coupled form,

$$\frac{\partial \vec{V}}{\partial t} + \left(\vec{V} \cdot \vec{\nabla} \right) \vec{V} = -\vec{\nabla} h + \vec{J} \times \vec{B} + \epsilon_\mu \nabla^2 \vec{V} \tag{15}$$

$$\frac{\partial \vec{B}}{\partial t} = \vec{\nabla} \times \left\{ \left[\vec{V} - \epsilon_H \vec{J} + \epsilon_A \vec{J} \times \vec{B} \right] \times \vec{B} \right\} + \epsilon_\eta \nabla^2 \vec{B} \tag{16}$$

Where advective terms – such as the very Hall term – are responsible for cascade

mechanism: dissipative processes operate on B and V due to coupling. The scaling parameters,

$$\epsilon_H := \alpha \frac{c/\omega_{pi}}{L_0} = \alpha \frac{\delta_i}{L_0} \tag{17}$$

$$\epsilon_A := \epsilon_H \frac{\omega_{ci}}{\nu_{in}} \tag{18}$$

$$\epsilon_\eta := \eta \frac{t_0}{L_0^2} = \frac{\eta}{L_0 V_0} \tag{19}$$

$$\epsilon_\mu := \mu \frac{t_0}{L_0^2} = \frac{\mu}{L_0 V_0} \tag{20}$$

serve to show the parameter dependence. It is important to note that the Hall scaling parameter is enhanced by a factor of $\alpha = \rho_n/\rho_i \gg 1$ in comparison with standard (fully ionized Hall term). One should also note that if all scaling parameters are zero, we have the ideal limit.

Upon defining the Reynolds number as ratio of advective term and dissipation term, and define Kolmogorov scales by viscosity, resistivity dissipation, or ambipolar diffusion, we can estimate appropriate Kolmogorov scale determined by balance between relevant energy cascade and dissipation mechanisms, when plasma parameters and energy injection rate are specified.

Krishan and Yoshida computed [8] a table that illustrates the significance of each regime for each set of parameters, as shown in table 1, and this is useful for when we are ready to examine the conditions for the plasma to generated for the present project,

Dissipation mechanism	MHD regime ($\epsilon_H K < 1$)	Hall MHD regime ($\epsilon_H K > 1$)
Viscosity	$K_\mu = \xi^{1/4} \epsilon_\mu^{-3/4}$	$K_{\mu H} = (\epsilon_H^{-1})^{1-q} K_\mu^q (< K_\mu)$
Resistivity	$K_\eta = \xi^{1/4} \epsilon_\eta^{-3/4}$	$K_{\eta H} = \epsilon_H K_\eta^2 (> K_\eta)$
Ambipolar	$K_A = \xi^{1/2} \epsilon_A^{-3/2}$	$K_{AH} = \epsilon_H^{-2} K_A^{-1} (< K_A)$

Table 1. Pertinence of energy dissipation mechanisms in a weakly ionized plasma.

One can therefore obtain:

a) The variation of ionization fraction ρ_i / ρ_n with distance. This was engaged in this work with a first approach of diagnostics.

b) The variation of ratios $K_A / K_{\eta, \mu}$ and K_η / K_μ with distance for different values of injection rate ξ . This will be engaged in the future, when independent ion measurements can be carried out. At a certain distance we can choose parameters as normalization for calculating V_0 and ξ .

1.5 Design of a New Device and Objectives

Further exploration of the weakly ionized plasma regime is necessary for deepening the understanding of plasma processes and energy dissipation mechanisms. As the last section shows, parameters such as the ionization ratio are important to situate oneself in a specific domain where the prevalent energy dissipation mechanisms might be otherwise veiled.

A new device has also been proposed for allowing a wider flexibility of operation in comparison with the RT-1 dipole device, where the magnetic source can be exchanged for a solenoid and varied according to convenience. The usage of a supported permanent magnet as a source of magnetic field can both accomplish this and also allow a not so cumbersome implementation of an electric field towards plasma flow and a possible connection with the

studying of astronomical accretion disks.

Such a project envisaged as its first objective the planning and construction of the device, as well as the generation of an ECH plasma in it. A last stage was left for the implementation of diagnostics for a basic characterization of the plasma produced, towards an increased efficacy of measurements and testing of the regimes of low-ionized plasma. Key parameters of the plasma produced will therefore be the electron temperature in a radial profile, and the plasma density likewise to try to find ourselves in agreement with the original considerations of the frameworks under Hasegawa and Yoshida-Mahajan.

The new device and its implementation is described in the following section.

Chapter 2
Experimental Set Up

As in the previously-discussed experiments that produce plasma using ECH waves, the magnetic field source has been mounted on the equatorial plane from a top flange in the center with movable belows, in line with an arrangement of ports for the implementation of diagnostics – a Langmuir probe initially –, a pumping station and ports for observation as well as one port for driving RF waves into the He-filled vacuum chamber.

The injection of gas is made possible from another top flange through a needle valve above a security valve for avoid breaking the vacuum in case the needle is broken upon closing it beyond the limits of its spring.

The vacuum vessel, a stainless steel chamber has a radius of 0.6 m and a height of 0.9 m. These dimensions were considered to encompass the greater possible region of the plasma to be confined by the central permanent magnet.

The chamber also has six lateral ports, as well as seven upper and seven lower ports. In total, the chamber has a volume of 1.14 m^3 when considering the protrusion of ports out of it and the extra section added by the pumping station.

This chapter deals with the considerations undertaken for each of these parts involved. Figure 1 shows the overview of the mounting of the experiment. Figures 2 and 3 show pictures of the actual experimental set up as it was being prepared.
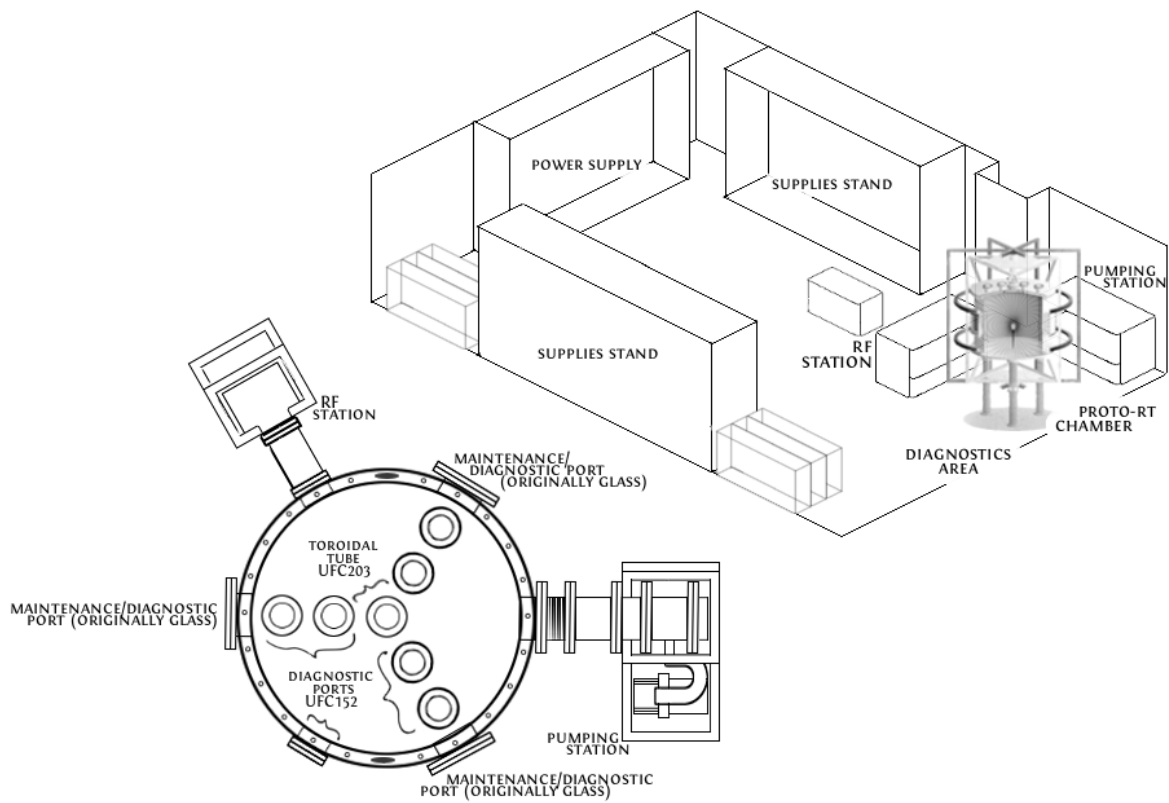
Figure 1. General layout of the experiment, focusing on the disposition of the space and usage of the ports of the chamber.
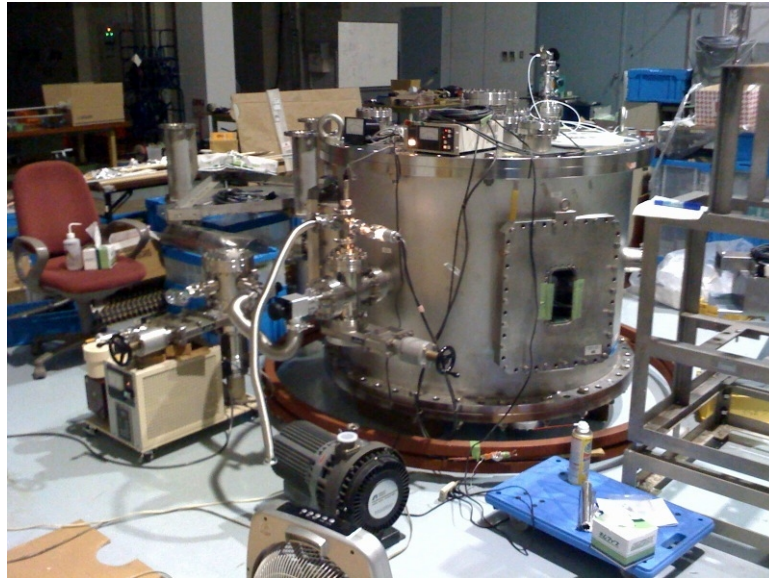
Figure 2. Pumping system and observation port side of the vacuum chamber. The
turbomolecular pump can be observed to the left, and pressure gauges on top.

Figure 3. RF system and gas injection side of the vacuum chamber. On the
bottom side the RF system can be seen along with its waveguide.

2.1 Pumping System Performance and Gas Feed

For the evacuation of filling gas, an ULVAC YTP-m turbomolecular pump with a pumping speed of 150 L / s was used. The turbomolecular pump is connected to a backing rotatory pump, and both their performances for the respective vacuum chamber were tested. Figures 2 and 3 show the results obtained, and it can be seen that the rate of evacuation of air gives away the presence of some leaks that modify the expected decay inversely proportional to time. In the ideal scenario (where Q = 0),

$$-VdP/dt = PS - Q \tag{21}$$

$$P(t) = Q/S + (P_0 - Q/S)\exp(-St/V) \tag{22}$$

where V is the volume in liters, P is the pressure, S is the evacuation speed in Ls^{-1} and Q are the leakages. In this way the expected filling gas pressure was of the order of 10^{-6}. Figures 4 and 5 show a non-exponential behavior, so we assume some considerable leaks. However, they are small enough that a background filling was pressure in the order of 10^{-5} Torr can be obtained, which is good for the generation of plasma in our conditions, and altogether not that far from the expected one.

The turbomolecular pump in its system with the backing rotatory one possess emergency valves that are activated in case of a power outage to protect the blades of the turbomolecular pump from a possible threatening viscosity of the evacuated air. With regards to this, it is always necessary to start by pre-evacuating the chamber with a rotatory pump before turning on the blades of the turbomolecular pump. When the pressure reaches 90 Pa in the pumping station, the valves to the vacuum vessel are opened, assuring a safe operation environment. Once the overall pressure approaches 1 Pa, the turbomolecular pump blades are switched on. In practice, it takes a couple of hours to reach a pressure level of 10^{-2} Torr with the rotatory pump, while it takes around 24 hours until a 10^{-3} Torr pressure level is reached with the turbomolecular pump. After 2 days the desired background pressure for experiments of the order of 10^{-5} Torr is finally reached.
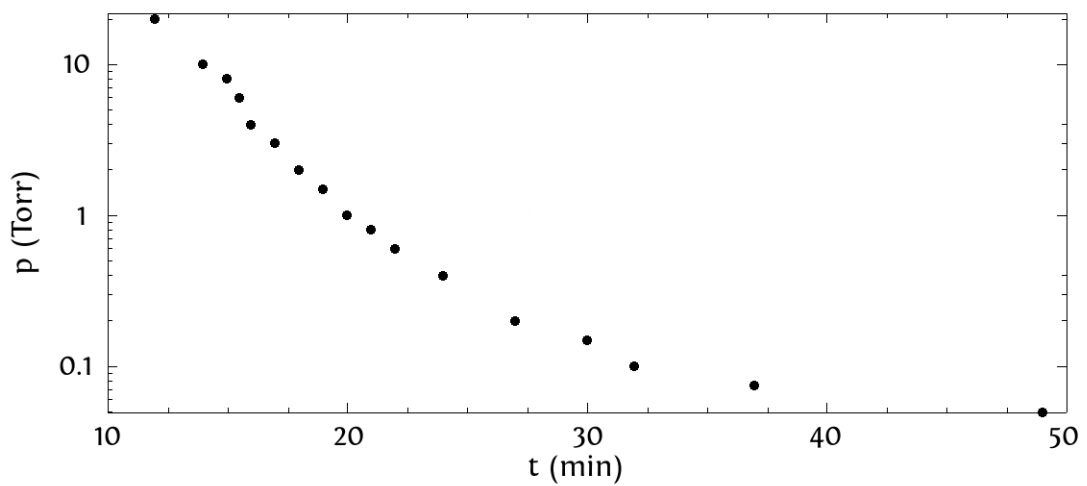
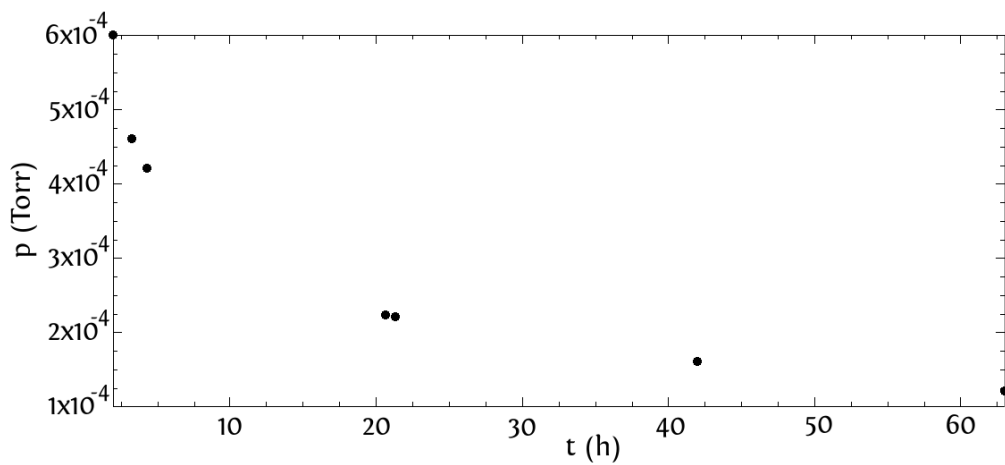Figure 2. Performance of rotatory backing pump.

Figure 3. Performance of turbomolecular pump.

Helium gas is injected through an Edwards LV10K needle valve for inert gas on an NW10 flange of one of the top ports of the chamber that is opposite from the pumping station. In this way we make sure there is He going through the magnet installed on the middle of the vacuum vessel. Helium gas was decided to be used due to its high second ionization energy of 54.4 eV which simplifies the analysis when looking for the ionization rates, even when Saha's equation is still required as discussed previously.

The operation with a hose connecting a Helium tank and the vacuum chamber requires for the washing of the hose each time before an experiment. To do this, the air in the hose was vented through a Helium rush evacuated by the pumping station.

A leak valve for ventilating the vacuum vessel was implemented as well. In the event of ventilating the chamber, it is suggested to use nitrogen was in order to avoid the condensation of water molecules and contamination.

The entire pumping system is illustrated in figure 4, where the ion gauges are seen on top of an NW40 cross tube together with the leak valve. The CF152 gatevalve on the lower side gives the possibility of attaching the turbomolecular pump system directly, with an auxiliar extra scroll pump for improvement vacuum conditions. Otherwise the gatevalve is kept closed and the turbomolecular pump operates through the flexible tube to the right end of the illustration. In this case the scroll pump is not operated simultaneously.

2.2 Pressure Gauges

The most basic measurement in the experiment was that of pressure. This was carried out through a pirani gauge for reliability above 10^{-2} Torr (pre-vacuuming stage), whereas an ion gauge with a hot filament was used for measuring the pressure throughout the experiments themselves in the 10^{-3} Torr range and lower. The ion gauge was found to give reliable measurements below 4×10^{-2} Torr in practice. A DC voltage applied to the electrodes of the gauge attracts the electrons from the gas which in turn ionize the gas molecules in the vicinity of the gauge acting as a charge collector, for a charge proportional to the number of molecules hitting its electrodes, which measure the level of pressure.
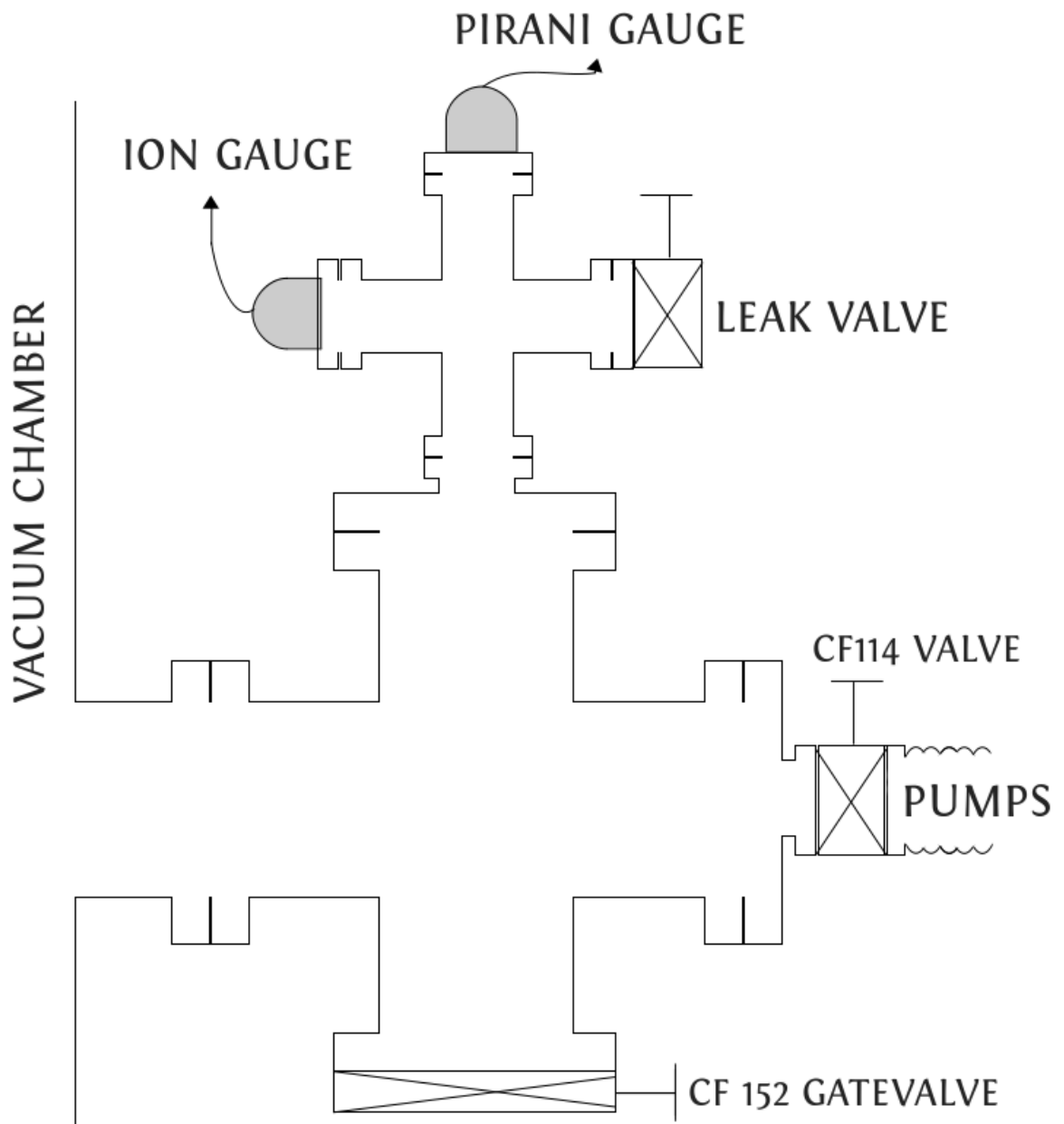
Figure 4. Pumping and pressure-monitoring system. The leak valve on top allows
for the refilling of the vacuum chamber for maintenance operations.

In order to extend the life expectancy of the ion gauge filament, its use is restricted to pressures of the order of 10^{-3} Torr. This is due to its nature as a charge collector and demands for the same vacuum conditions as a light bulb would.

For the pressure range considered, and the volume of 1.14 m³ of the chamber, at ambient temperature, the He molecules have an initial free path of ~1 m in ambient temperature conditions, which is of the order of the dimensions of the vacuum vessel. These are the initial conditions inside the vacuum vessel before RF waves are launched and plasma is generated. Background filling gas pressures were for all successful experiments of plasma generation around 5.4×10^{-5} and 1.1×10^{-4} Torr.

2.3 Magnetic Field Source

As mentioned earlier, the source of magnetic field in this case was a permanent rare earth magnet. A cylindrical neodymium magnet producing a magnetic field of the order of 1000 G (or 0.1 T), and of a diameter of 10 mm and height of 12 mm was chosen in order to set the magnetic surfaces of 845 g for ECH resonance of electrons, in which orbit for that magnetic force they resonate with the 2.45 GHz waves injected from the lateral side of the cylindrical magnet.

Neodymium was chosen because of its good performance at high temperatures of hundreds of °C and its remanence of around 1 T, and was protected with a stainless steel case from direct contact with the plasma to be produced. The magnet was mounted on a central upper port with bellows to fix its position accurately in the very center of the vacuum chamber locked by a stainless steel rod. It's alignment was checked through the diagnostic ports which are aimed at the center of the vacuum vessel.

The actual measurement of the magnetic field produced by the permanent magnet was performed with a Honeywell SS94A2D ratiometric Hall sensor mounted on a side port. This was needed to determine the sensitivity according to each applied bias voltage. Figure 5 shows the principle of the sensor in its interaction with the dipole field. The P-type semiconductor sensor is shielded and requires of VCD power supply. Since its operating

temperature is up to 125 °C, it is possible to operate it under plasma conditions. The sensor's sensitivity was indicated as 1.00 ± 0.02 mV / G, however it was necessary to measure it in practice for each input voltage applied in order to see how many volts of Hall output voltage equate to how many gauss. Opposite faces of the Hall sensor measure opposite polarity, with face opposite to circuit having greater efficiency and measuring north pole as a positive voltage output or Hall voltage V_H.
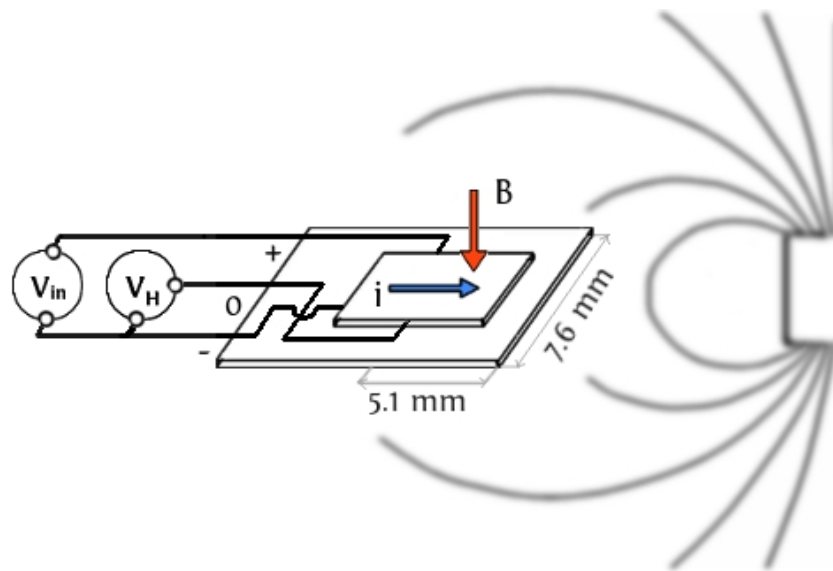

Figure 5. Hall sensor used for the empirical measurement of the magnetic field, with sensitivities of the order of 1.00 mV / G (depending on V_{in} used).

The Hall sensor works by the hall effect, where a charge buildup on the sides of circulating current (driven by the input voltage across the Hall element), generates an output Hall voltage proportional to the magnetic field. This proportionality is to be established by calibrating the Hall sensor with a double Helmholtz coil with a number of turns n=68, outputting a known and homogeneous induced magnetic field dependent on n and the current that circulates through its turns. Thereby testing for a range of currents between 0.5 and 4.0 A − inducing respective magnetic fields of 4.1 to 34.5 G −, it was possible to estimate the sensitivity of the Hall sensor at different input voltages. The graphs in figure 6, 7 and 8 show the calibrations

used for obtaining the equivalence between the Hall voltage obtained at a multimeter and the magnetic field that it corresponds with, for each input voltage at the Hall sensor.
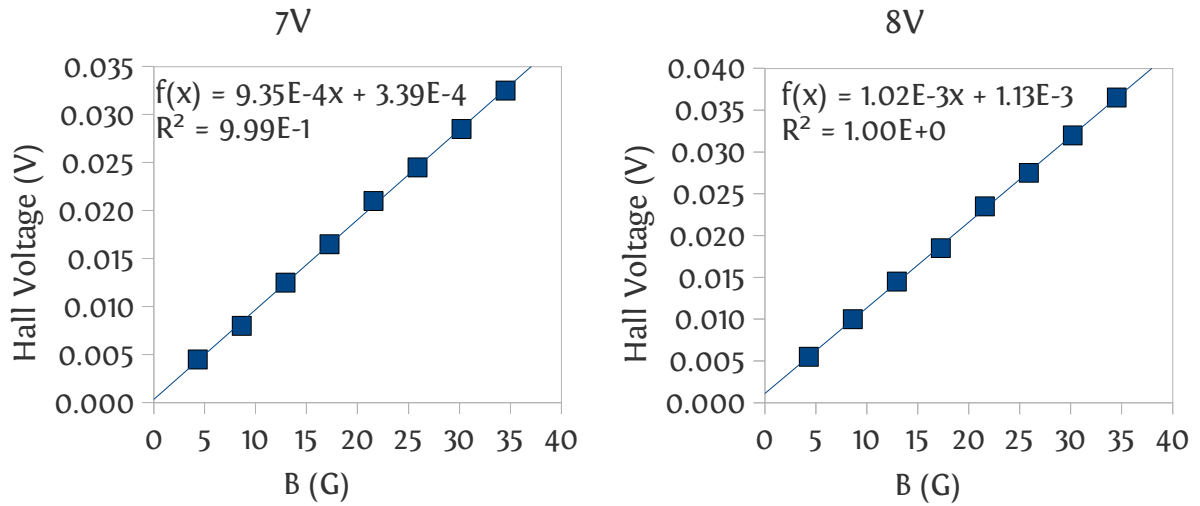
7V

8V

$f(x) = 9.35E\text{-}4x + 3.39E\text{-}4$
$R^2 = 9.99E\text{-}1$

$f(x) = 1.02E\text{-}3x + 1.13E\text{-}3$
$R^2 = 1.00E\text{+}0$

Figure 6. Hall sensor calibrations for input voltages of 7V and 8V.

9V

10V

$f(x) = 1.19E\text{-}3x + 4.64E\text{-}4$
$R^2 = 9.97E\text{-}1$

$f(x) = 1.30E\text{-}3x + 7.86E\text{-}4$
$R^2 = 9.99E\text{-}1$
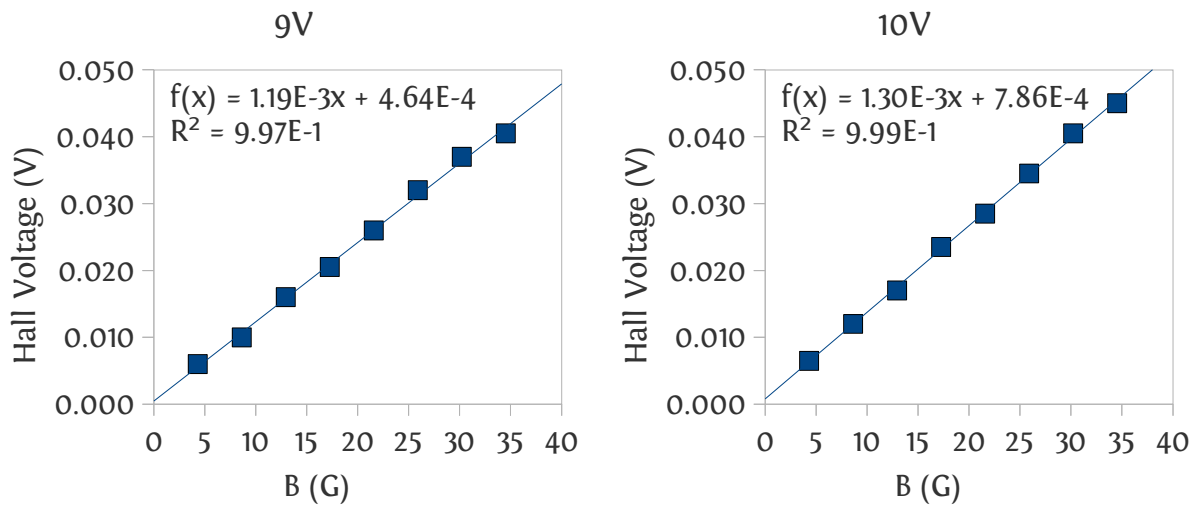
Figure 7. Hall sensor calibrations for input voltages of 9V and 10V.

11V

f(x) = 1.28E-3x + 2.09E-3
R^2 = 9.97E-1

12V

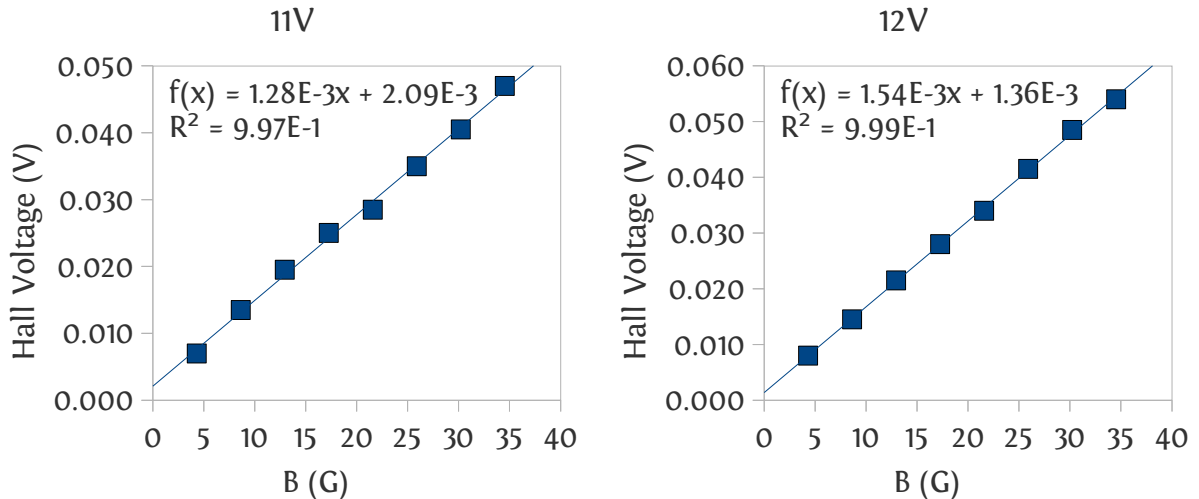f(x) = 1.54E-3x + 1.36E-3
R^2 = 9.99E-1

Figure 8. Hall sensor calibrations for input voltages of 11V and 12V.

We see that magnetic field strengths of tens of G are recorded in the Hall sensor as tens of mV, and that the relations are very accurately lineal, which gives a high degree of confidence performed. As can be seen in figure 5, the nearness of the Hall sensor to the geometrical center of the configuration (the axis of the magnet) is limited both by the magnet's body itself (i.e. its 5 mm of radius) and the edge of the chip on which the Hall element is mounted, leaving its center 10.1 mm away from the geometrical center when performing radial measurements of the magnetic field. On the opposite radial direction – i.e. away from the magnet – the Hall sensor outputs voltages that rapidly become smaller and smaller when measured in an oscilloscope, until becoming too noisy to be reliable. At this point the noise becomes comparable with the measurement.

Figure 9 shows the magnetic field as measured empirically with the Hall sensor. The measurements were performed for 7, 8, 9, 10, 11 and 12 V of input voltage, with the respective calibration values of figures 6 through 8.

The decline of the field strength with the distance agrees well with the rapid decrease expected in a dipole field approximation of the r^{-3} order. Because a larger region is of interest for the plasma experiments upon seeking for radial profiles, a projection is made from the field measurements of figure 9 in figure 10. It can be observed that the field strength peaks

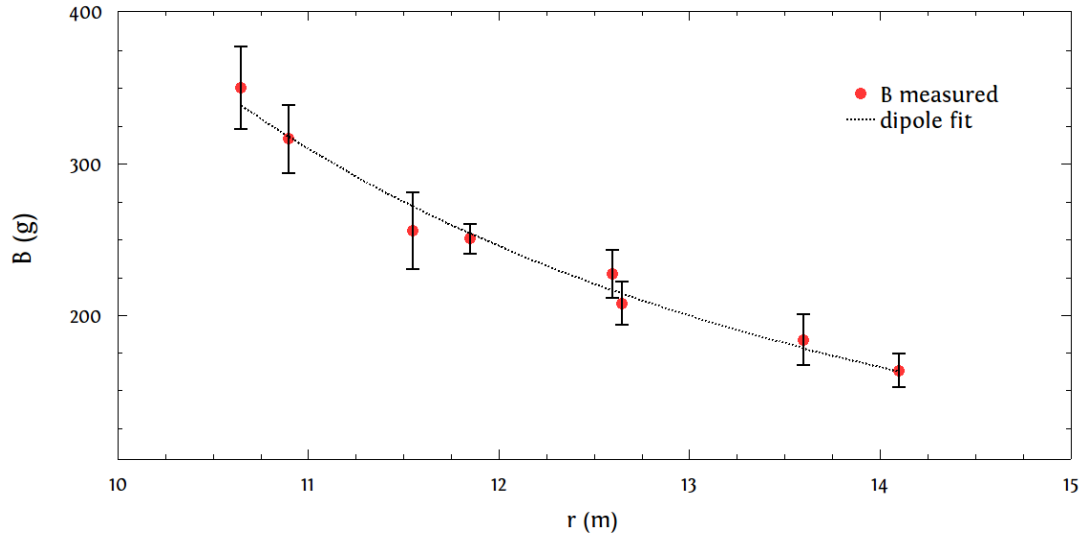rapidly as it nears the surface of the magnet.

Figure 9. Magnetic field measurement with a Hall sensor, averaged
for a sweeping of voltages in the 7-12 V range.

The extrapolation gives that the layer for 2.45 GHz ECH resonance lies 2.6 mm outside the surface of the magnet. Therefore it is possible to use ECH as a method for plasma production through particle-resonance interaction. At that position the field strength has a magnitude of 845 G, therefore the electron cyclotron frequency,

$$\omega_{ce} = \frac{eB}{m} \tag{23}$$

matches the RF power frequency when operated in the 2.45 GHz mode. It has to be noted that the dipole approximation used for the extrapolation of the magnetic field measured does not apply very close from the axis of the magnetic field source, but this still gives us the indication that ECH heating can be achieved at a layer near the magnet's surface.
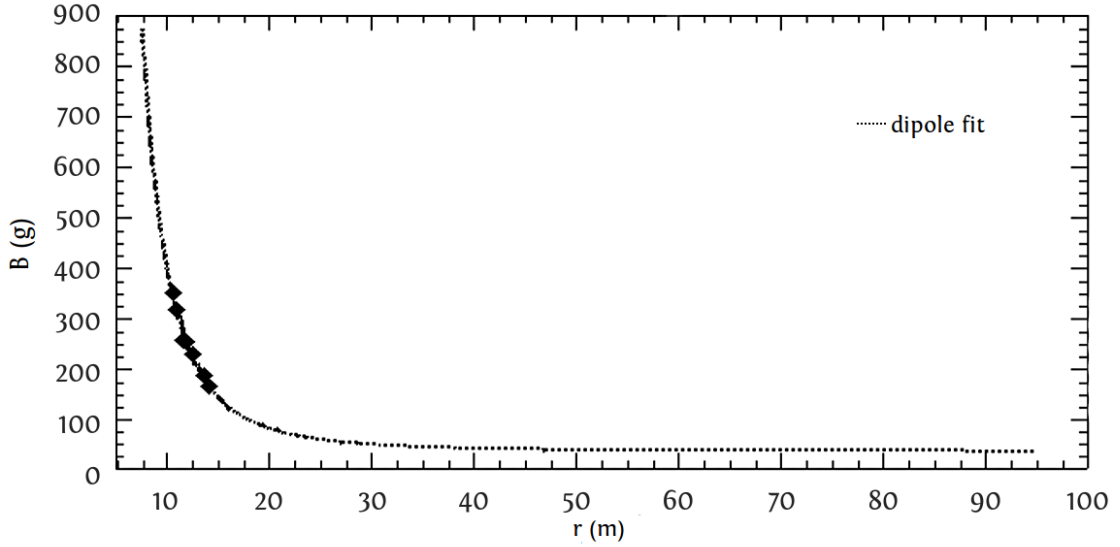
Figure 10. Projected magnetic field measured with a Hall sensor.

In figure 11 we present the Larmor radius for electrons,

$$r_L = \frac{m\,v_\perp}{|q|\,B} \tag{24}$$

in the near field region around the magnet for different possible orders of the electron temperature, if it is assumed that the kinetic energy is roughly distributed in the perpendicular direction with respect to the magnetic field.

Although as noted in the introduction, the gyro motion is just one of three movements of charged particles in a dipole field, this tells us that the electrons heated by ECH close to the magnet's surface will acquire an amplitude of movement of the order of 1 cm for one of its periods (the others being the bounce motion and the drift motion in the toroidal direction). Thus upon a successful production of plasma by ECH resonance in the region close to the magnet's surface, one can expect a high temperature plasma sheath of some cm thick.
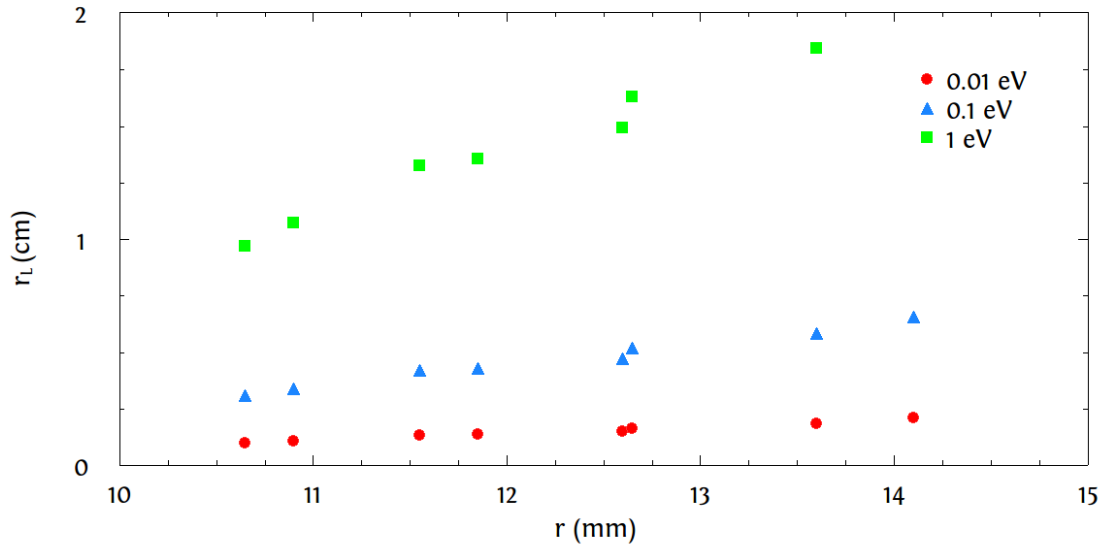
Figure 11. Larmor radius for electrons in the magnetic field
measured for electron temperatures of 0.01 eV, 0.1 eV and 1 eV.

2.4 RF System and Plasma Generation

For the feeding of 2.45 GHz RF waves, a 5 m long transmission line from 220 V of the main power source was connected to a magnetron power supply IDX IMP-15ENA running on 2 A. This in turn connects to the magnetron oscillation unit which RF output power has a maximum of 2 kW, and produces waves at a frequency of 2.45 GHz.

Finally, the oscillation unit is connected to a window port at equator plane towards the permanent magnet through a rectangular waveguide which dimensions are impedance-matched. Its height is half its width, in order to maximize the power that can propagate inside of it before dielectric breakdown occurs. The O-mode was used, given the parallel orientation of the electric field through the waveguide and the orientation of the dipole magnetic field. This means that in the outline of the RF system used in this experiment shown in figure 12, the electric field is in the vertical direction as is the dipole field generated by the magnet.
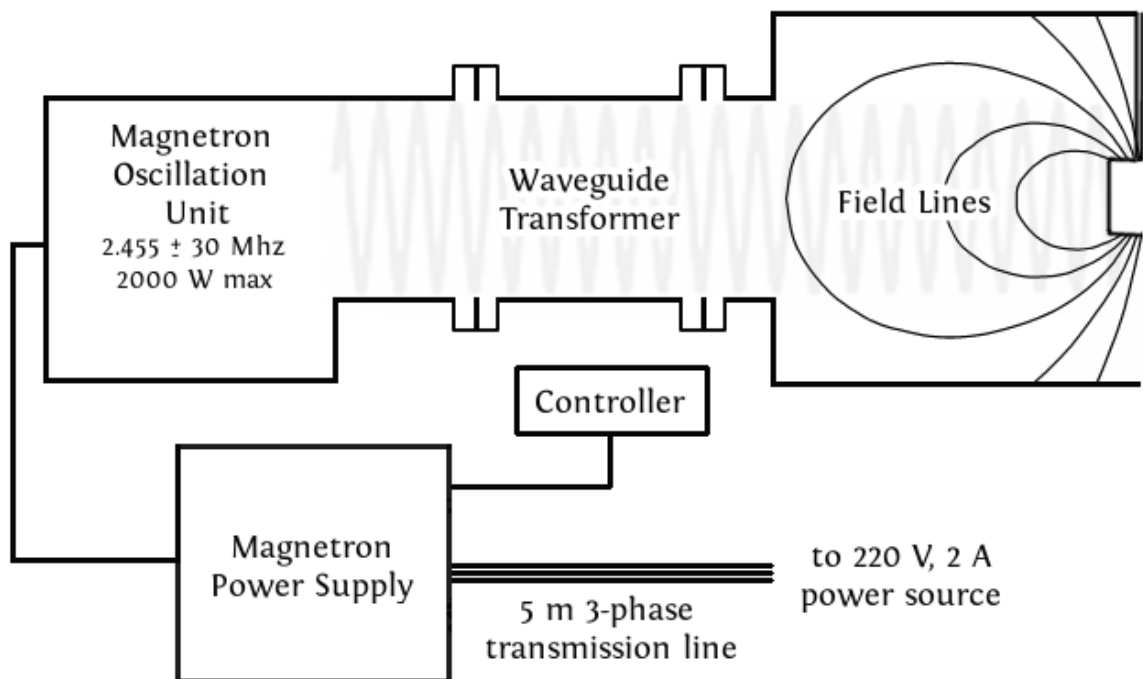
Figure 12. RF system used for driving 2.45 GHz O-mode waves into the dipole field region for generation and heating of plasma.

The dimensions of the waveguide – which are advantageous in this case for permitting propagation with lower loss than coaxial cables – are 110 mm x 55 mm for the above-mentioned necessity of impedance matching. The recommended frequency band for this case is 1.72 to 2.60 GHz. When frequencies are lower than 1.5 GHz, the waveguide dimensions become too large (the higher frequency, the smaller the waveguide's dimensions needed), and for higher frequencies than 330 GHz, the dimensions become too small to be technically convenient.

The principle of ECH heating and plasma production through it is described in detail by Landau damping, where it is characterized thanks to the cold plasma model. Essentially, it gives a condition for resonance that the electron gyrofrequency must be matched to the frequency of the RF source. At a magnetic field of about 875 Gauss, the electron Larmor frequency of 2.45 GHz. At sufficiently low pressures, the electrons gain energy on each orbit around the field lines. So the field provides for confinement and efficient electron heating.

In the collisionless damping process in which resonant absorption takes place, the latter does not depend on collisions. Important here is rather an understanding of cutoffs and resonances, which have to do with the values of the refraction index n in the plasma, through the wavenumber k. They refer to those values where the wave propagation features are qualitatively altered.

When $k_\perp^2 = 0$ is reached through the change in plasma parameters – which is equivalent to them making $n_\perp^2 = 0$ – we say that a cutoff takes place, in which case the wave becomes evanescent. That is to say, it declines exponentially and wave penetration is stopped. This turns important in this experiment, due to observations in which plasma was generated merely in the RF port (right hand side of the wave transformer in figure 12).

In the opposite case, when the plasma parameters turn $n_\perp^2 = \infty$, large energy absorption takes place, as the energy flow is slowed giving way to decreased dissipation. Although the cold plasma model does not include the mode conversion processes through which plasma heating can also be achieved, this on itself shows a considerable part of the realistic scenario that is to take place upon successful plasma heating through ECH waves injection.

It must also be noted that the cyclotron frequency is above the plasma frequency, that is to say,

$$\omega_{ce} \geqslant \omega_{pe} \tag{25}$$

we will only be heating electrons – at least through direct resonance, since mode conversions can also take place – through electron cyclotron waves.

If the density surpasses a critical limit, ECH waves are unable to further penetrate to central regions, such as the surrounding regions of the permanent magnet itself.

In the O-mode that we use, the propagation is described – always according to the cold plasma dispersion relation – as [28],

$$n_{\perp}^2 = 1 - \frac{\omega_{pe}^2}{\omega^2} \tag{26}$$

from where the accessibility condition comes out as,

$$\frac{\omega_{pe}^2}{\omega_{ce}^2} = l^2 \tag{27}$$

where l is an integer that indicates which level (from fundamental to n-level harmonics) is excited. The fundamental resonance of O-mode is due to the finite electron Larmor radius effects of a hot plasma. The O-mode does not depend on the launching and if the density is below the cutoff value, then it will freely penetrate towards the resonance region that we have determined to be located 2.6 mm from the magnet's surface.

Using only ECH as our source for plasma, and doing so in low power for our exploration of weakly-ionized plasma production, it is unlikely for us to expect high beta values. On this regard, ECH can produce beta values below $0.004\, l^2\, Te(keV)$ in the O-mode case.

2.5 Langmuir Probe and Circuit

Upon successful generation of plasma, the next step is its characterization, in order to examine its profiles and determine whether it is of use for the studying of the weakly-ionized regime as has been planned for.

A useful diagnostics technique in this case in which we operate with low temperature plasma is the Langmuir probe, devised by Irving Langmuir in 1924. In general, Langmuir probes make use of how the plasma behaves as part of an electric circuit when made to interact with electric fields or voltage differences from an external diagnostic system. More specifically, it consists of examining the current-voltage characteristics' reaction of the plasma when an electrode set to a – usually floating – potential is introduced in it, and a potential swept is performed from negative to positive values. This I-V profile can be used to determine the electron temperature, the plasma components' densities, and the plasma potential, depending in which Langmuir configuration is selected.

In our case, we have constructed a Langmuir probe as the one shown in figures 13 and 14, extending from the diagnostics port of the vacuum vessel, pointing towards the center. An alumina ceramics tube – which provides for insulation to several hundreds of °C – protrudes 40 mm from a stainless steel tube. Tungsten wires go from the outside end of the probe to the end where it is to meet the plasma. The idea is to shield the tungsten wires with the ceramics, and also to constrain the surface through which they are exposed to the plasma, as they will act as the charge collectors from it. At the same time, the ceramics assure us that corrosion from the stainless steel tube will not ensue if it was left to interact with the plasma directly, something which could pollute it.

Tungsten is itself chosen as the charge collector from plasma due to its high melting point and corrosion resistance. Inside the steel tube which is 820 mm long, the tungsten wires are replaced by copper wires insulated with teflon, for avoiding temperature effects in their conduction. All of these shielding considerations are important because at least part of the probe was to be directly exposed to the plasma. On the opposite end, the wires are connected to the circuit shown in figure 15.
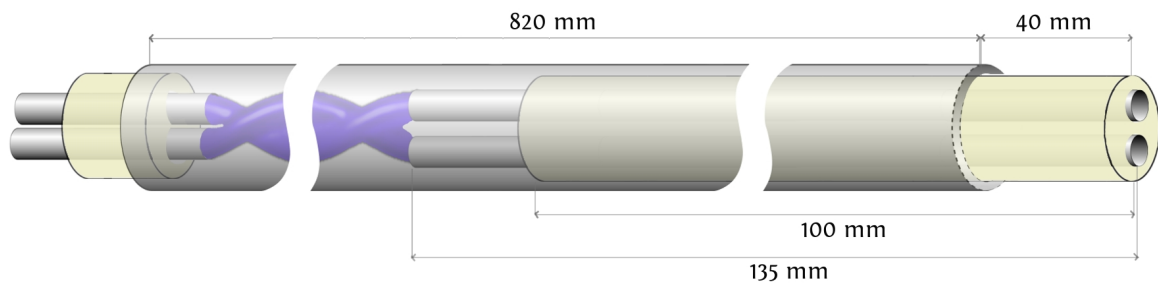
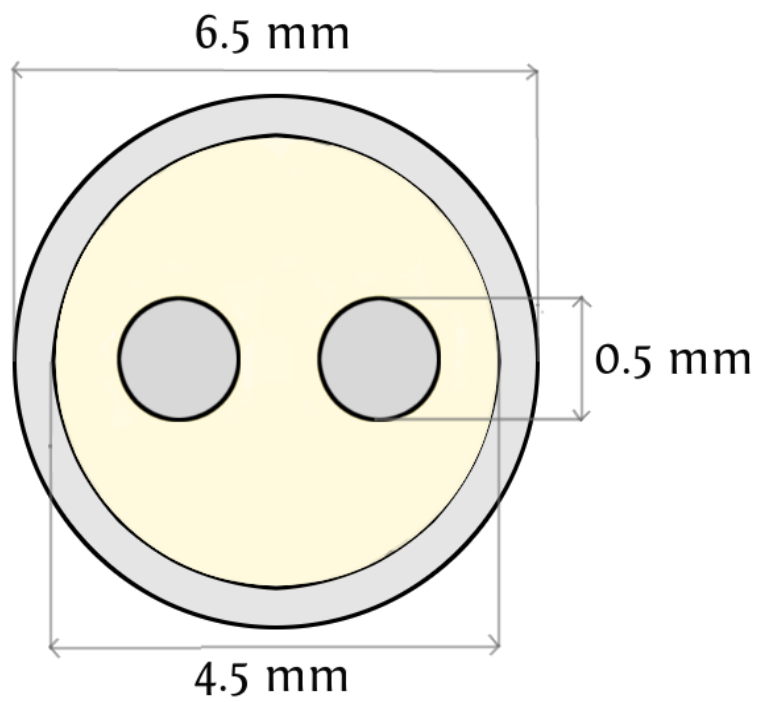Figure 13. Double Langmuir probe dimensions, lateral view.

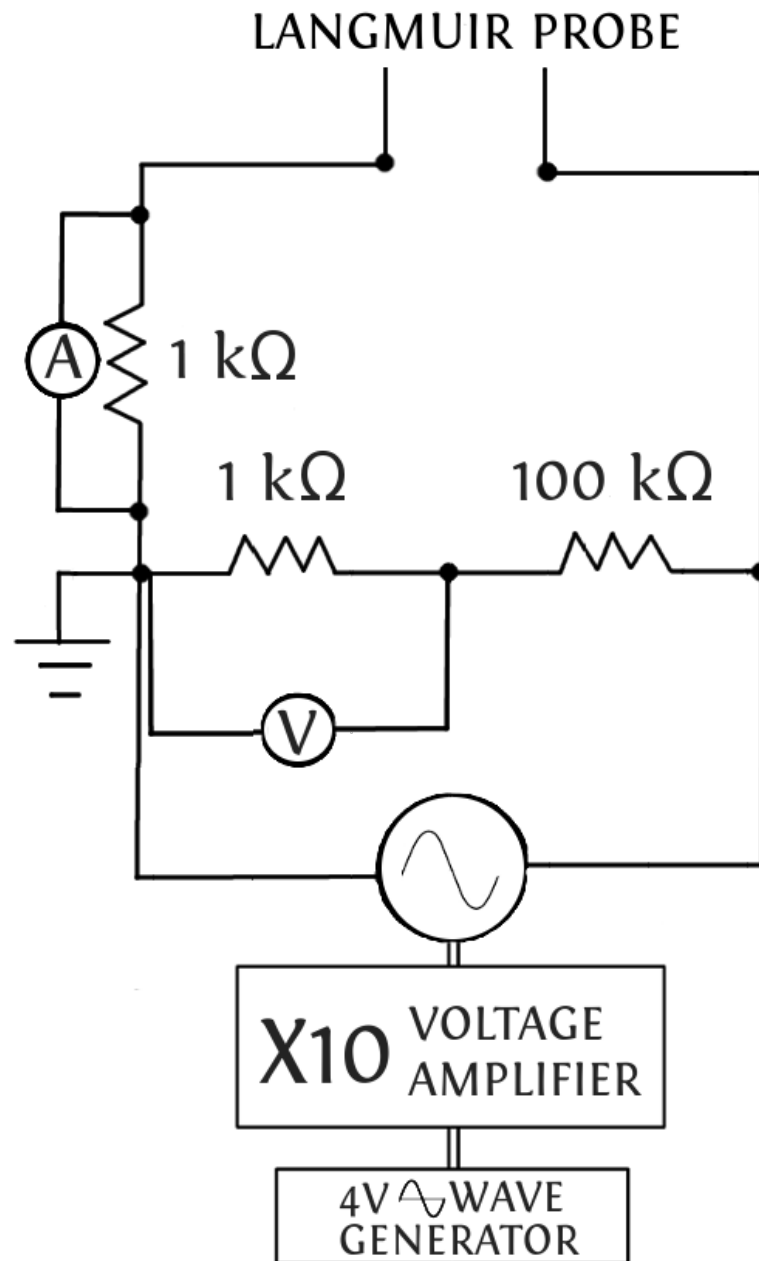Figure 14. Langmuir probe dimensions, cross section.

Figure 15. Langmuir probe circuit used, where current is measured through a voltage probe in parallel with a 1 kΩ resistance. The voltage used was 40 V.

A Langmuir probe constructed in such a way is known as a double probe. And the reason why we have chosen this configuration is because double probes provide direct measurements of electron temperature, and most importantly in our case in which a plasma of a small scale length and low temperature was expected, because when using double probes, one avoids that the probe becomes a significant loss area of plasma from the system [31]. This is due to the fact that the potential applied through such a double probe is fully a floating potential.

When the two Langmuir probes – our tungsten wires portions exposed to the plasma – are biased to a certain potential, the entire system floats, there existing no net current. The flow of current thus obtained is measured as a function of bias voltage, making it possible to determine electron temperature and plasma density.

2.5.1 Determination of the Electron Temperature

The electron temperature shall be determined first. From the condition that the system be floating, in a double probe we can determine the electron temperature from the morphological properties of the I-V profile through [30],

$$\left(\frac{di}{dV}\right)_{V=0} = \frac{e}{kT_-}\frac{i_{1+}i_{2+}}{i_{1+}+i_{2+}} \tag{28}$$

where the first term refers to the slope of the curve in the origin. Here the currents refer to the ion (+) currents in either side of the voltage sweeping (negative and positive sides), and can be determined as the projections of the saturation currents towards the axis. So we determine the electron temperature as,

$$T_- = M_0\frac{e}{k}\frac{i_{1+}i_{2+}}{i_{1+}+i_{2+}} \tag{29}$$

where M_0 is the inverse of the slope at the origin.
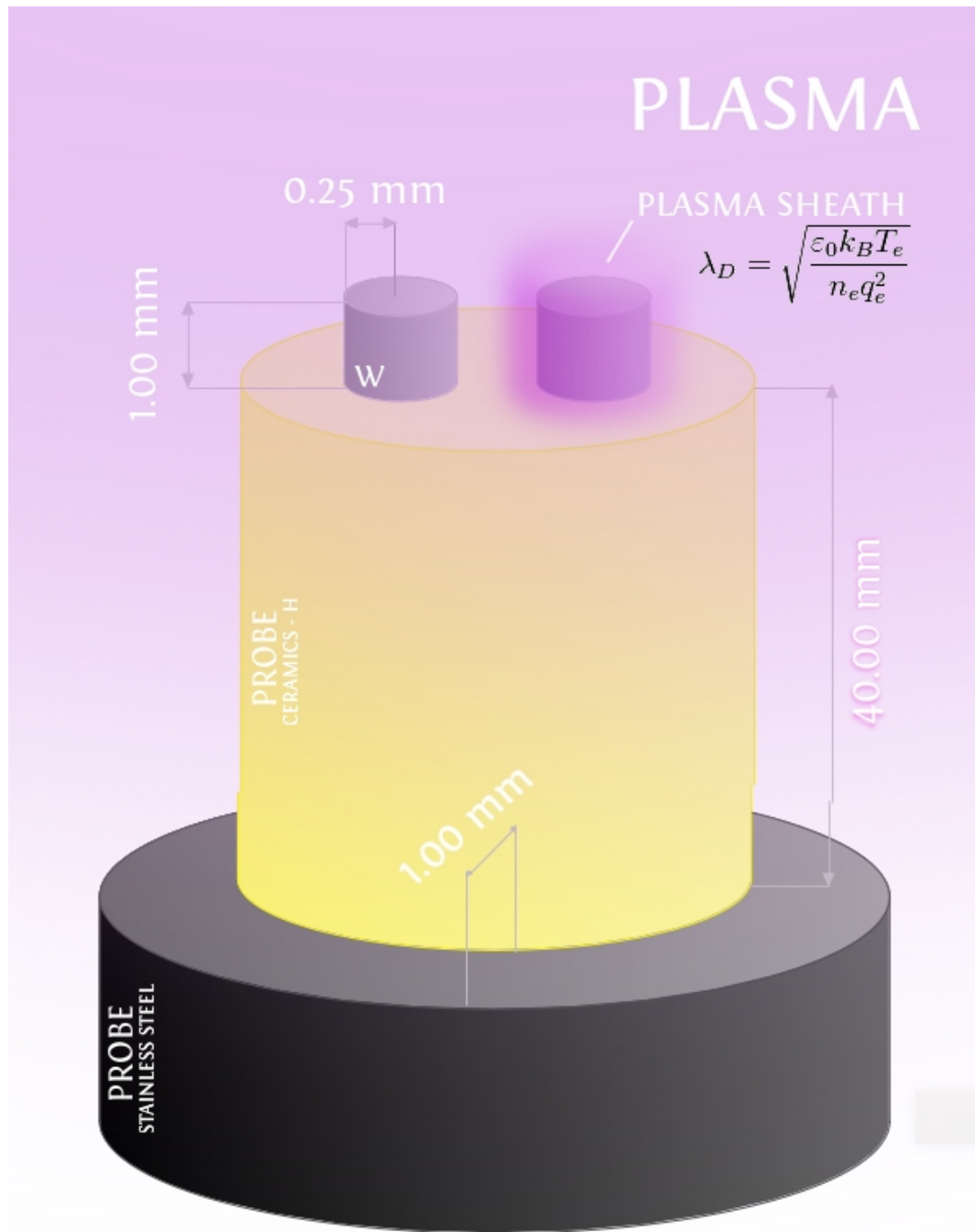
Figure 15. Langmuir probe circuit used, where current is measured through a voltage probe in parallel with a 1 kΩ resistance. The voltage used was 40 V.

2.5.2 Determination of the Plasma Density

From here, the plasma density can be computed through theories of ion collection and determined in function of the electron temperature and the surface of the probe S as,

$$i_{Bohm} = 0.61\, n\, e \left(\frac{k T_e}{m_{He}} \right)^{1/2} S \tag{30}$$

where i_{Bohm} refers to the averaged saturation current, and m_{He} is the atomic mass of Helium in our case. The factor 0.61 is due to the reduction in the density of the ions in the presheath forming around the electrodes of the probe – our wires – which is the region over which ions are accelerated up to the Bohm speed. [30]

The equation for ion saturation for determining the density is from the Bohm current case, which amounts to the case in which $T_- \gg T_+$, and not from ion thermal speed. What is happening is illustrated in figure 15, in which our probe is introduced in the plasma, and a plasma sheath around the tungsten wires forms with a thickness of the order of the Debye length. In our case the surface area is 1.77×10^{-6} m^{-2}.

The I-V characteristic obtained from our probe is going to be affected by the electrons' speed being much higher than the positive ions' speed due to their inertia. Due to this, determining the temperature of the ion components of the plasma is not possible with this kind of diagnostic.

Chapter 3
Results and Analysis

Plasma was obtained for the first time at Helium gas pressures of 10^{-2} Torr and RF power of 0.20 kW. Different regimes were observed as pressure drops from the high end of 10^{-2} Torr until 10^{-3} when the discharge finally disappears, and were also swept for a range of RF power applied between 0.05 kW and 0.38 kW, all for background pressures $\sim 10^{-5}$ Torr.

Upon experimentation, it was realized that there was a leak of RF waves, since placing a fluorescent tube by the side of some of the ports would ignite and heat it. In consequence, security measures were established for the electromagnetic sealing of the ports that presented leaks, making use of small Faraday cages mounted on the outside, wrapping up the viewports.

3.1 Plasma Configurations

Figures 16 to 20 show digital pictures of the different plasma configurations obtained by examining a series of pressure and RF power combinations (the order of images goes from higher to lower gas filling pressure). Figure 16 shows the first scenario, in which plasma is solely produced on the side of the RF port, at a pressure of $p = 9 \times 10^{-3}\,Torr$ and 0.15 kW of RF power. This might seem the case discussed in the previous chapter, which the density is too high for accessibility conditions to give way for wave penetration to the central regions.

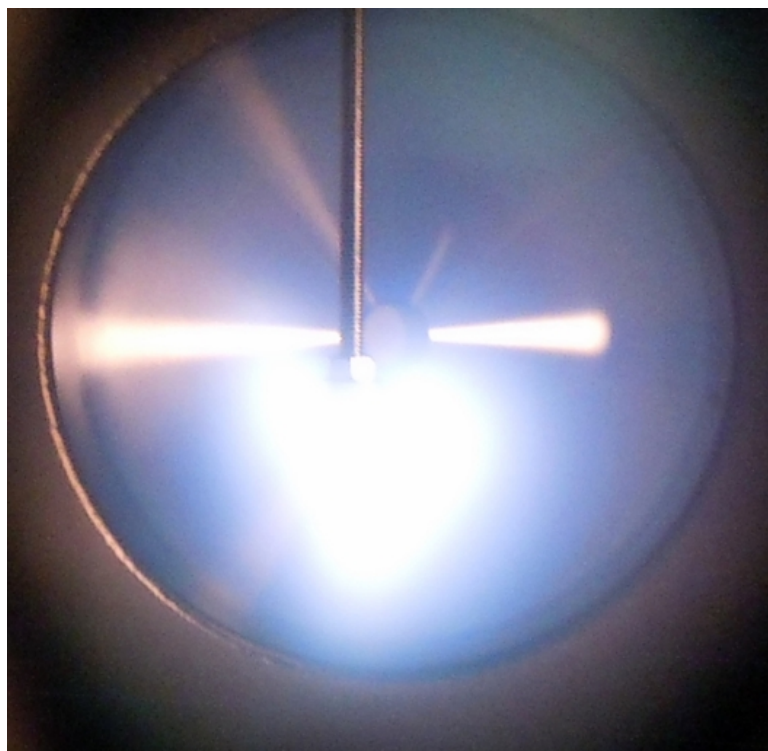Figure 16. Plasma on port for $p=9\times10^{-3}\,Torr$, $P=0.15\text{kW}$.

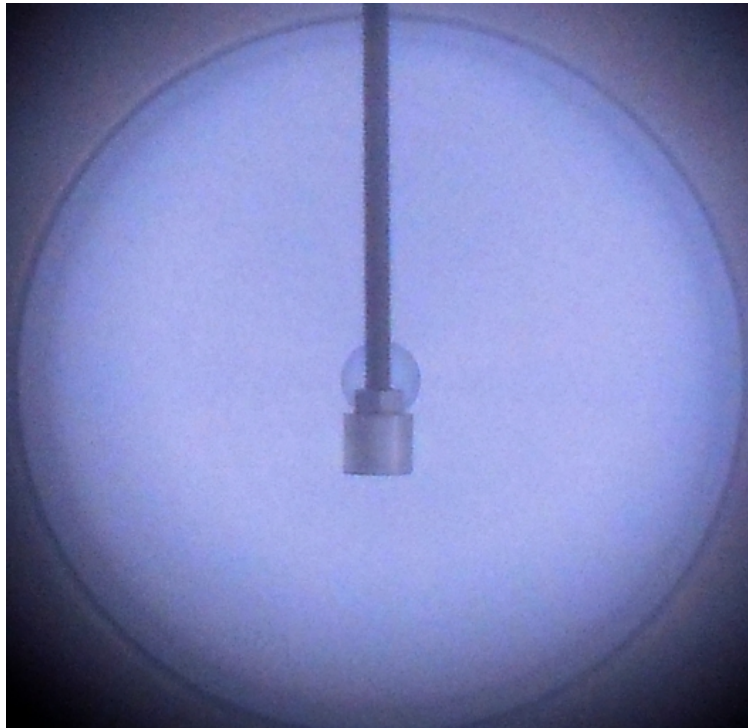Figure 17. Plasma around magnet for $p=8\times10^{-3}\,Torr$, $P=0.15\text{kW}$.
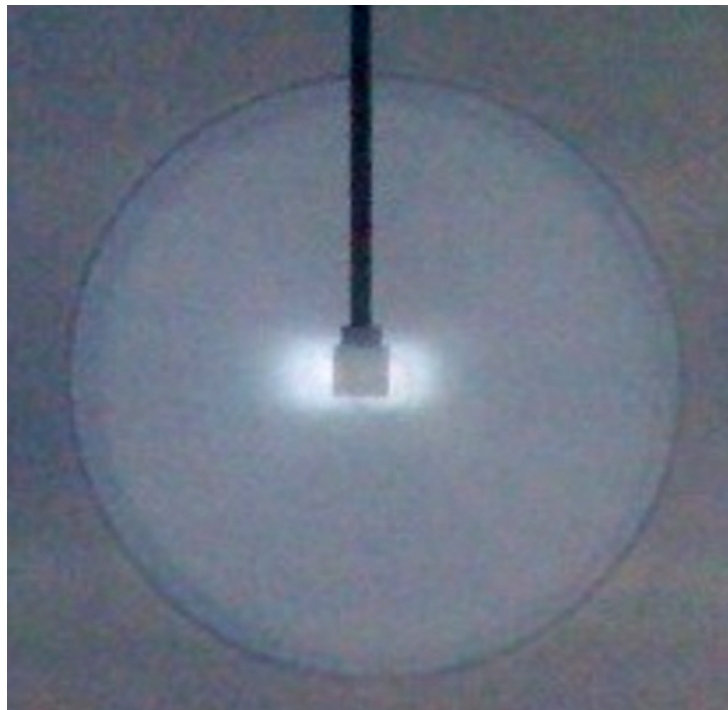
Figure 18. Plasma glow for $p=7.2\times10^{-3}\,Torr$, $P=0.05$kW .

Figure 19. Plasma glow and centering for $p=5.4\times10^{-3}\,Torr$, $P=0.05$kW .
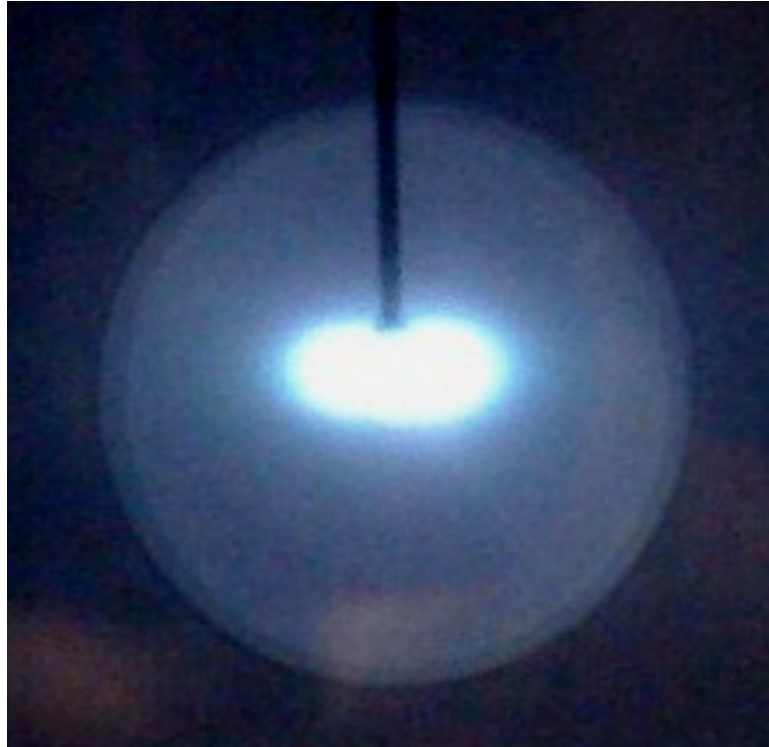
Figure 20. Plasma focused around magnet, $p=3.3\times10^{-3}\,Torr$, $P=0.10\text{kW}$.

Figure 17 corresponds to what seems a transition phase between the plasma generated on the RF port and plasma that might be generated by ECH heating in the central region. We note that this process of ionization seems necessary for the production of plasma. It can be observed that the confinement does not even fit with the typical dipole shape we would expect with the magnet that we have as our magnetic source. Yet the plasma is still trapped around the magnet in an area expanding some 3 cm. Why the plasma is trapped around the magnet – as if it was responding to the magnetic field strength – but not according to a dipole shape is an interesting question, and at such high pressures of operation of $p=8\times10^{-3}\,Torr$, it could be telling us that neutral components are playing a role, since we assume ionization is very low at that stage and neutrals vastly overwhelm ions. It will be shown later that this is indeed the case, with the Langmuir probe measurements.

Figure 18 shows the plasma configuration generated for $p=7.2\times10^{-3}\,Torr$ and RF power of 0.05 kW. This scenario has been labeled as "glow" through this section, as the entire

vacuum vessel seems to glow under these conditions without a visible central plasma structure forming around the magnet. This "glow" will be used as a comparison with the case in which a clearly higher temperature and more dense plasma is formed around the permanent magnet.

Figure 19 shows another stage of transition, this time between the "glow" scenario and the case in which the plasma is completely focused around the magnet. In this transition case, around $p=5.4\times10^{-3}\,Torr$ and 0.05 kW of RF power applied, plasma begins to focus around the magnet in what we could call a more dipole-like configuration or responding better to it. This indicates a higher ionization rate, where charged particles seem to be making up a more significant part of the plasma than for the case described in figure 17. It turns out that this stage of plasma configuration is the one which allows the most flexible variation of filling pressure and RF power applied. All other stages are comparatively narrow with respect to these parameters.

Finally, figure 20 shows the case in which most of the observable plasma is focused around the magnet in a quite distinguishable magnetospheric configuration for $p=3.3\times10^{-3}\,Torr$ and 0.10 kW of RF power. A blue hue is common when this structure is formed. In general the tone seems to go from pink to blue and white as the He filling pressure decreases.

With the purpose of mapping these configurations in a pressure-RF power phase space, and determining regimes of operation for these parameters, both pressure and power sweepings were performed, from higher to lower pressure and from lower to higher RF power.

The results can be seen in figure 21. There, the labels port, port-focused, glow, glow-focused, and focused refer to the visible structures described in figures 16, 17, 18, 19 and 20 respectively, and the color is a representation of the visual appearance of these plasma configurations.

As can be observed, there is a wide area in the pressure-power phase space to study the case in which the plasma begins to focus around the permanent magnet. It is this area that has been selected for the Langmuir probe measurements and will be studied in detail in the following section.

But before that, it is interesting to note the narrow domain in this phase-space for the latter

case described above, that is, the case in which the entirety of plasma seems to focus as a magnetosphere in the center. This state was particularly unique, because although it could be achieved with low RF power, it seemed to correspond with the largest leaks of electromagnetic noise, such as when placing a fluorescent tube in its vicinity, or when taking pictures of it with a digital camera − the latter would suffer noticeable interference only in this case.
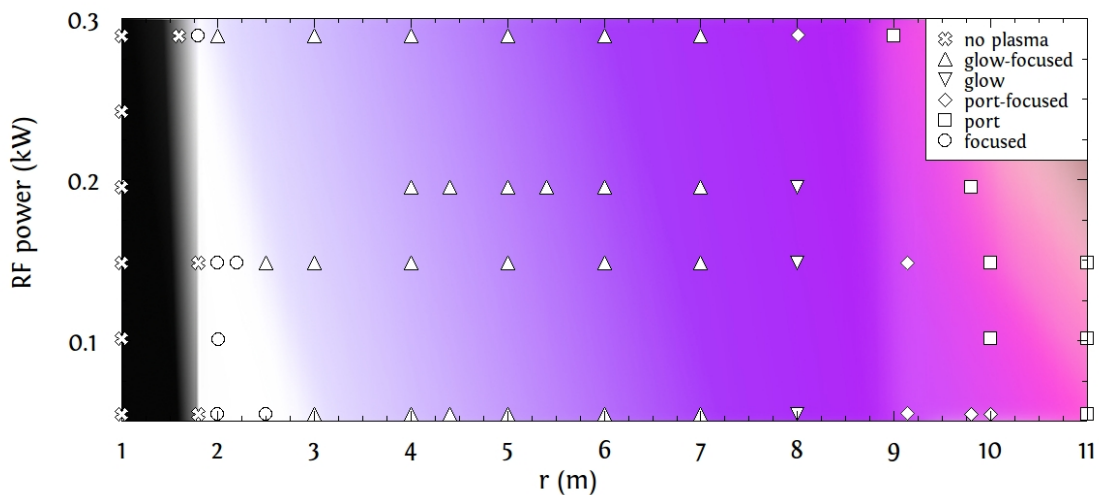

Figure 21. Plasma configurations in pressure-power phase space.

This phase-space that was mapped would seem to indicate that at high pressures, on the edge of our spectrum, the density is sufficiently high to produce early cutoff regions that prevent the ECH waves from penetrating deeper into the plasma. In fact, measurements of reflected and incident ECH waves showed that in these cases the reflected waves were quite significant, up to an 80% of the incident wave. This could be accounting both for reflection and successive mode conversions taking place.

It should be noted though, that for the cases of lower pressures, we have achieved indeed a seemingly magnetospheric configuration as we were pursuing, and the characterization of these plasma structures are detailed in the below section on Langmuir probe measurements for them.

3.2 Langmuir Probe Measurements

As discussed above, the pressure-power domain chosen for Langmuir probe measurements is that described for figures 18, 19 and 20, (that is to say, gas filling pressures in the $p=3 \sim 7 \times 10^{-3} Torr$ and $P=0.05 \sim 0.25 kW$ range) at which a plasma that responds to the confinement of the central magnetic field seems to be present.

In measurement with our Langmuir probe, voltage was swept in a sinusoidal wave from -40 V to 40 V.

In order to interpret the results obtained from our probe measurements, it is necessary to stop on the ideal probe features. We first notice that the current we measure is the sum of currents from ion and electron components of the plasma in which the probe is immersed. In the case of a Maxwellian distribution of ions at T_{+} , the ion current collected from ions depends on the bias voltage V_B according to [31],

$$i_{+}(V_B) = \begin{cases} -i_{+,sat} \exp[e(V_P - V_B)/kT_{+}], & V_B \geq V_P \\ -i_{+,sat}, & V_B < V_P \end{cases} \tag{31}$$

where V_P is the plasma voltage and $i_{+,sat}$ is the same saturation current discussed in equations (28) and (29). This expresses the collection of charge for values of V_B that are close to V_P since we see from (31) that a much larger value of the bias voltage causes no current, which is due to the fact that ions begin to be repelled from the probe for the case $V_B > V_P$.

Similar, but of opposite nature, is the case for the collection of electrons in the probe, which is going to be superimposed with the ion collection on the final current measured by the Langmuir probe. In the case of electrons, the current depends on V_B for an electron temperature T_{-} as,

$$i_{-}(V_B) = \begin{cases} i_{-,sat} \exp[-e(V_P - V_B)/kT_{-}], & V_B \leq V_P \\ i_{-,sat}, & V_B > V_P \end{cases} \tag{32}$$

The addition of these two cases is represented in figure 22, for the ideal probe features observed in a Langmuir probe I-V profile (in arbitrary units for the current). The saturation currents can be identified from the left and right ends of the I-V profile and coincide with horizontal lines as expected from equations (31) and (32) for the cases in which $V_B > V_P$ and $V_B < V_P$ respectively. However, as mentioned in the previous section, the ideal case on the left-hand side of figure 22, with the current actually saturating, is rarely observed, due to the expansion of the sheath that forms around the wires of the probe, an expansion that increases for increasing V_B. Therefore, the right-hand side of figure 22 is closer to the real probe features observed.

The saturation currents on both ends turn out to be parallel as discussed for equations (28) to (30).
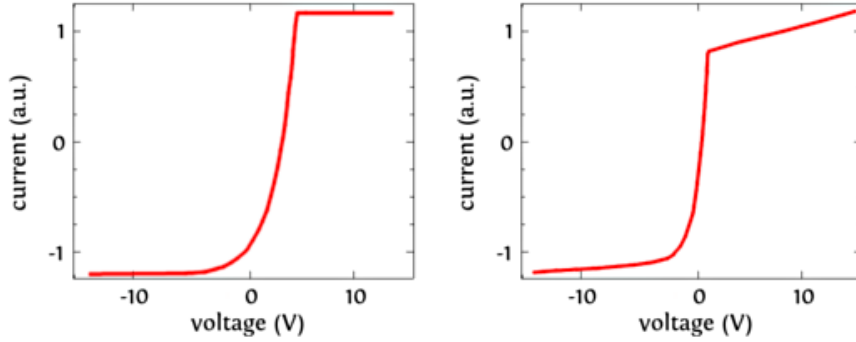

Figure 22. Ideal probe I-V features for a case where there is an effective saturation current (left side), and a case where there is no saturation (right side).

In both cases of figure 22, the current is greatly amplified in order to distinguish the inflection points of the I-V profile, which are necessary to the analysis of our measurements. We identify the lower current end $-i_{+,sat}$ from equation (31) (that is, the left side of the I-V profiles of figure 22), with i_{1+} in equations (29) and (30), and the upper current end $i_{-,sat}$ from equation (32) (that is, the right side of the I-V profiles of figure 22), with i_{2+} in equations (29) and (30).

Therefore we notice that the analysis of our measurements focus on the coefficients of three linear equations, which can be seen as the tangents to $-i_{+,sat}$, $i_{-,sat}$, and the middle inflection $(di/dV)_{V=0}$ as required in equation (28). In the first two cases, we are interested in the value of the saturation current at which these tangents intersect the axis, while for the third case, we are interested in the slope.

Typical results of the data and its analysis in order to obtain the electron temperature and density are shown in figure 23. The raw data can be seen in figure 23-a where current rises in the order of tens of μA correspond to the AC voltage sweeping used for the probe. As can be observed, about six cycles of voltage sweeping – from -40V to +40V – were recorded for each measurement.

Notice that only one cycle is necessary for a I-V profile, therefore the remaining five cycles can be considered to improve the statistical accuracy of the measurements when taken into account.

Figure 23-b is a first-layer treatment of the raw data, performed on the first sinusoidal cycle (one complete voltage sweeping) from figure 23-a, that is, from the first upper peak (corresponding to 40V) to the first lower peak (corresponding to -40V). To obtain this, a first order low-pass filter with a cutoff frequency of 250 Hz was applied for a first removal of noise. As expected from figure 22, inflexion points are observed around the middle of the I-V profile, and the ends at both sides follow the same increasing fashion of the right-hand side image in figure 22, corresponding to 'saturation' currents which increase as the voltage rises, indicating the expanding size of the plasma sheath formed around the tungsten wires of our double probe.

Here the saturation currents are indicated as L_1 (corresponding to $-i_{+,sat}$) and L_3 (corresponding to $i_{-,sat}$), and can be identified as the parallel lines that average the large span of data taken, as in the ideal case (figure 22). The slope of the I-V profile at its center, $(di/dV)_{V=0}$, is represented by L_2 , the line that intersects the saturation currents. Each of the lines represented in figure 23-b were obtained as the linear regression for the data points for each data range in which the behavior of the curve changes.
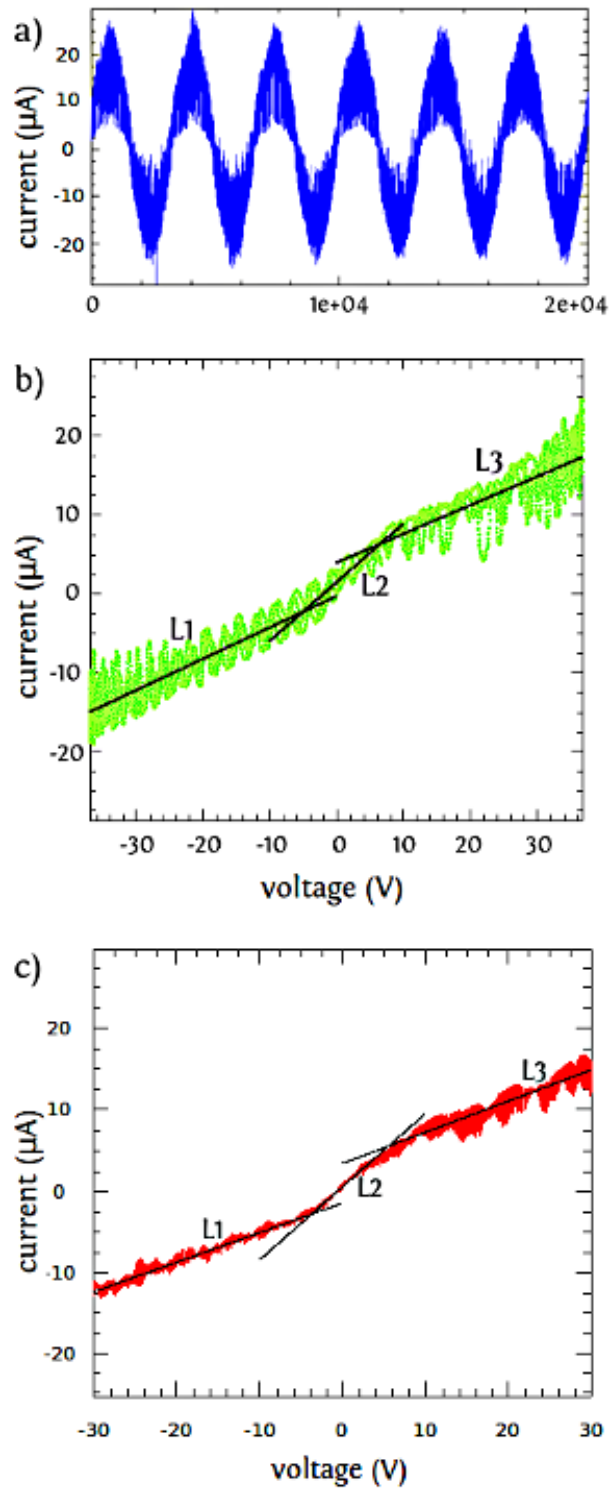
Figure 23. Raw data measurements (a) and I-V profile.

These values – i.e. the intersection on the current axis of the saturation currents' projections (L_1 and L_3)and the slope of L_2 at V=0 – are the ones used to evaluate the plasma parameters such as the electron temperature, the density and the ionization ratio throughout this section according to equations (29) to (30), and Saha's equation for the ionization rate. In figure 23-c further data treatment has been performed by applying a smoothing filter on top of the low-pass filter for further removal of noise and determining the more precise equations of the linear regressions. These turn out to be,

L_1: $i(V)=3.96\times10^{-7}V-6.23\times10^{-6}$,

L_2: $i(V)=7.42\times10^{-7}V+1.10\times10^{-6}$,

L_3: $i(V)=3.62\times10^{-7}V+3.61\times10^{-6}$,

for this specific sample case in which the power, pressure and distance of the probe from the center of the chamber were $P=0.25\,kW$, $p=3\times10^{-3}\,Torr$, and $d=7\,cm$ respectively. That is, a plasma configuration like the one observed in figure 19 in which there is a visible dipole plasma focusing in the center while a glow persists throughout the vacuum vessel. As can be seen, L_1 and L_3 are nearly parallel, as expected from the ideal case previously described for figure 22. From these three linear equations we obtain that $i_{1+}=-6.23\times10^{-6}$, $i_{2+}=3.61\times10^{-6}$, and $(di/dV)_{V=0}=7.42\times10^{-7}$. Therefore in this particular case, we obtain measurements of the electron temperature and density of $T_e=3.2\,eV$ and $n=1.7\times10^{15}\,m^{-3}$, which is along the expectations for a low-ionized plasma.

The same procedure described in the above lines was carried out for the six recorded cycles of each measurement, and 4 to 6 measurements for each set of RF power, He filling pressure, and probe distance conditions were performed in order to obtain radial profiles of the electron temperature and density with their according error bars.

3.2.1 Power and Pressure Dependence

Firstly, because of the noticeable effect of pressure and RF power on the visible characteristics of the plasma produced, it was examined with the Langmuir probes how these parameters impact on Te and n qualitatively. This in order to better assess the diagnostics of

the regimes of interest and whether comparisons with one another are valid or need to include the considerations that can be drawn from here. Figure 24 shows how T_e is affected by He filling pressure and RF power at a single point of measurement 7 cm from the magnet's surface, chosen here because it lies outside the region of "focusing" that could yield significantly different behaviors when changing the He pressure and RF power.
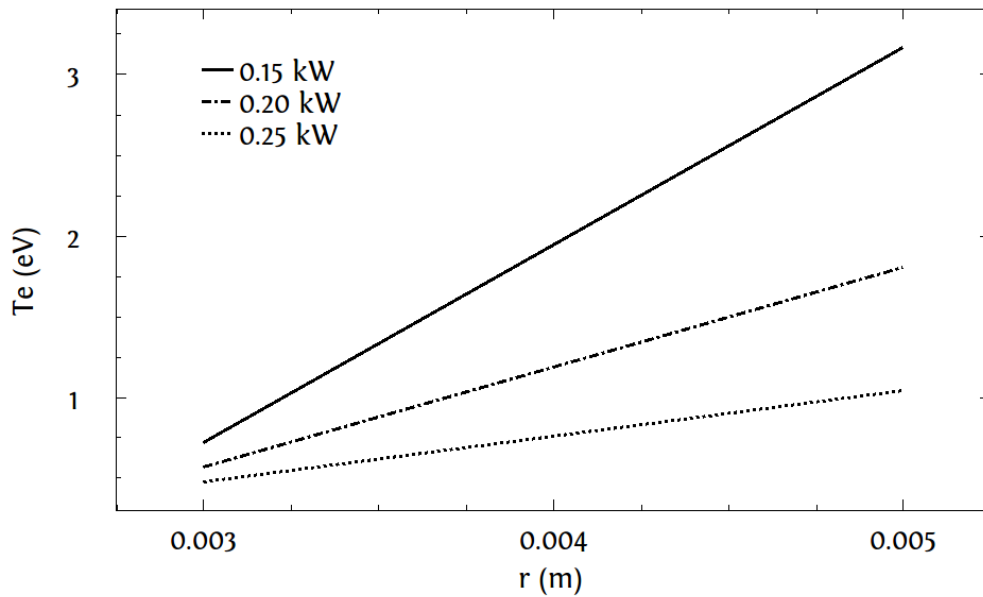

Figure 24. T_e at different gas filling pressures and RF power applied, at a fixed distance from the center of the magnet of 7 cm.

We obtain for the domain of interest, that higher pressure yields higher T_e. And for RF power, this proportionality holds true inversely. We obtain $T_e \sim 0.5$ eV for $p = 3 \times 10^{-3} Torr$ for RF power of 0.15, 0.20 and 0.25 kW. But when the pressure is almost two-folded to $p = 5 \times 10^{-3} Torr$ the electron temperature spikes more rapidly for the case of lower RF power, reaching $T_e \sim 3$ eV in this case, whereas RF power of 0.25 kW graces $T_e \sim 1$ eV. In figure 25 we see what happens with the density, at the same point located 7 cm from the surface of the magnet, under the same sweeping of pressure and power.
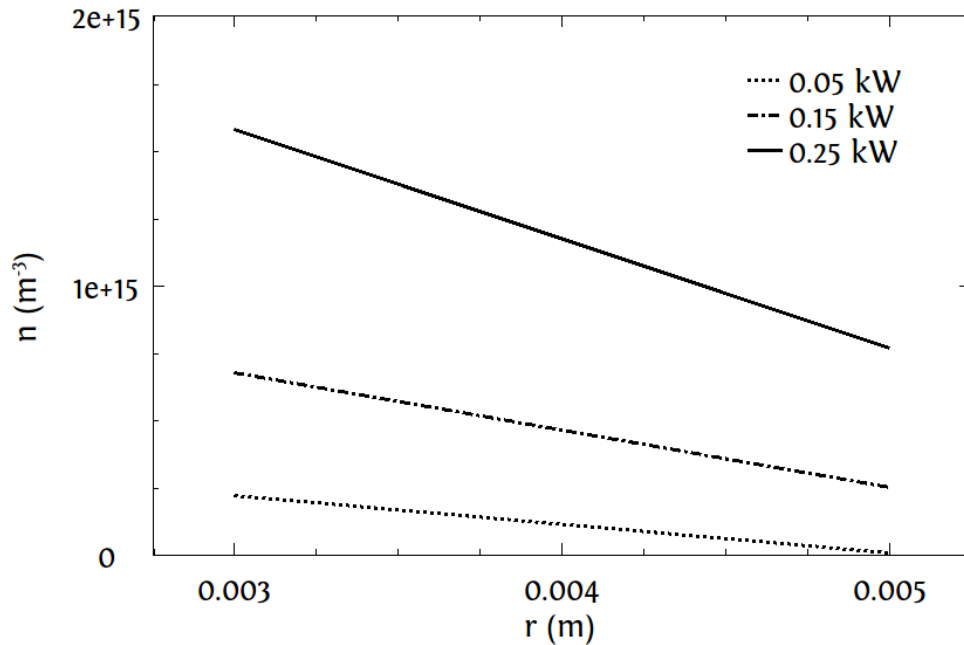
Figure 25. Plasma n different gas filling pressures and RF power applied, at a
fixed distance from the center of the magnet of 7 cm.

Now we see that higher pressures yield lower density, and this is inversely true for RF power injected. We obtain densities of the order of 10^{15} m^{-3} when using 0.25 kW, whereas for 0.05 kW and 0.15 kW the densities are in the 10^{14} m^{-3} order.

3.2.2 "Glow" Plasma Radial Profiles

The above-described behaviors are to be taken into account when building the spatial profiles of electron temperature and density, as well as when obtaining the ionization ratio throughout space.

On this latter regard, the radial profiles were constructed for the two cases in which there is only a "glow" and in the case where "focusing" in a magnetosphere-like shape is appreciated. It is necessary to take into account that these configurations occur for different He filling pressure and RF power, so in order to compare between them it is necessary to consider the pressure and power effect on the electron temperature and the density.

Figure 26 shows the electron temperature in space (always the radial direction), for the case of a "glow" plasma structure, and we observe that it decreases smoothly from 10 cm towards the magnet, with a spike at 4 cm. This seems to be the outer boundary of the focusing structure that begins to take place once pressure is lowered from the case in which plasma is only obtained on the RF port. Some diffusion could be taking place that accounts for the focusing on this boundary of the charged particles.
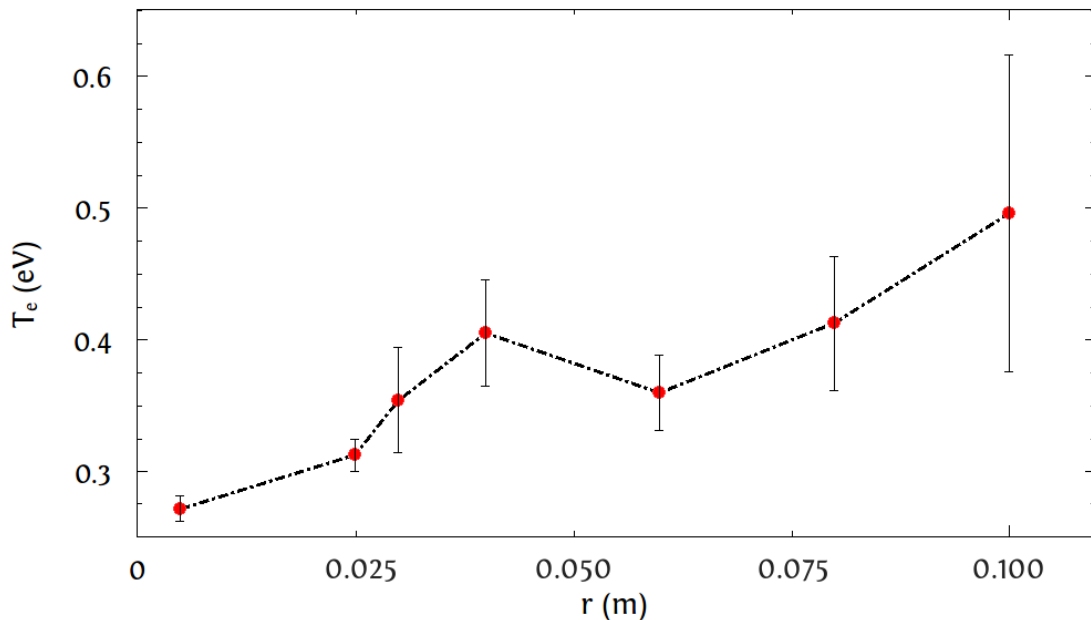

Figure 26. T_e spatial profile for a "glow" dipole plasma

at $p = 6.8 \times 10^{-3} Torr$ and 0.05 kW of RF power.

The electron temperatures are always within 0.3 eV and 0.5 eV, so one has to realize that the decrease is quite gradual. It is interesting to see that these electron temperatures express a considerable ionization, but not nearly as high as hot plasmas.

So this seems to be an indication – together with the magnetospheric-like configuration obtained – that we have obtained a suitable regime for the generation and study of low-ionized plasma.

Figure 27 shows the spatial profile of the plasma density which follows a similar trend as the electron temperature, with an increase of density as one moves away from the surface of the magnet and a sudden spike around 4 cm from it. The fact that the density is even higher 10 cm away from the magnet's surface, could be related to the formation of plasma in the RF port.
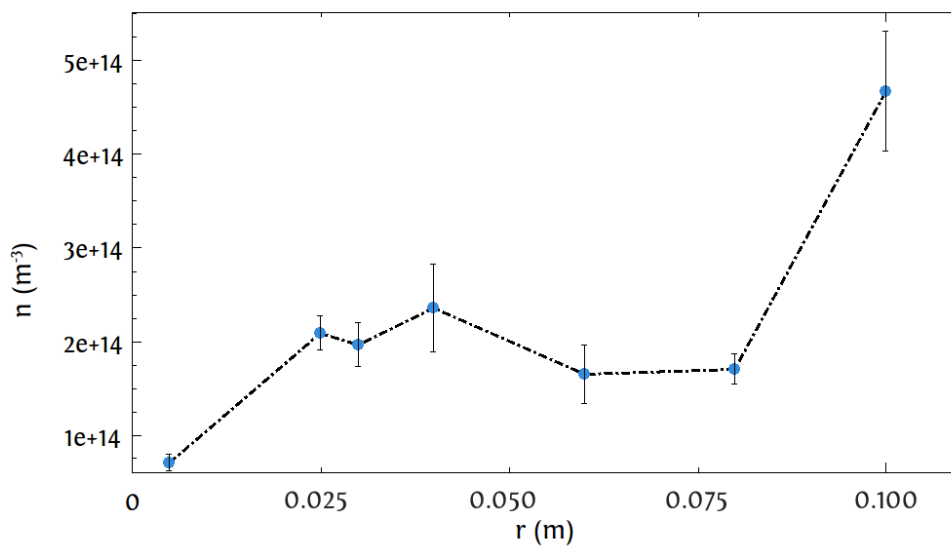

Figure 27. Density spatial profile for a "glow" dipole plasma at $p=6.8\times10^{-3}\,Torr$ and 0.05 kW of RF power.

We then see that the "glow" plasma configuration of the experiment is characterized by electron temperatures of a few tenths of eV, and densities between $1\times10^{14}\,m^{-3}$ and $5\times10^{14}\,m^{-3}$, which are normal values for cold plasmas.

3.2.3 "Focused" Plasma Radial Profiles

Moving on to the case in which plasma is "focusing" on the surroundings of the permanent magnet, the pressure decreases to $p=4\times10^{-3}\,Torr$ and the RF power increases to 0.25 kW. According to what we saw in figures 24 and 25, decreasing the He filling pressure and increasing the power result both in lower electron temperatures and also both in higher

density. To evaluate this, we present the Langmuir-probe-measured-profiles for these parameters in figures 28 and 29, in comparison with the "glow" case.

We notice for the electron temperature (figure 28), that it is in general lower in the case of a "focused" structure when far from the magnet, as expected by the previous consideration according to the lower pressure and higher RF power. But as we approach the magnet, the "focused" plasma case presents a significant peak in electron temperature which saturates as one moves further towards the magnet and falls. The distance at which this occurs is slightly below 1 cm, within the region of ECH resonance. This seems to indicate that charged particles with higher energy become confined in those particular regions.
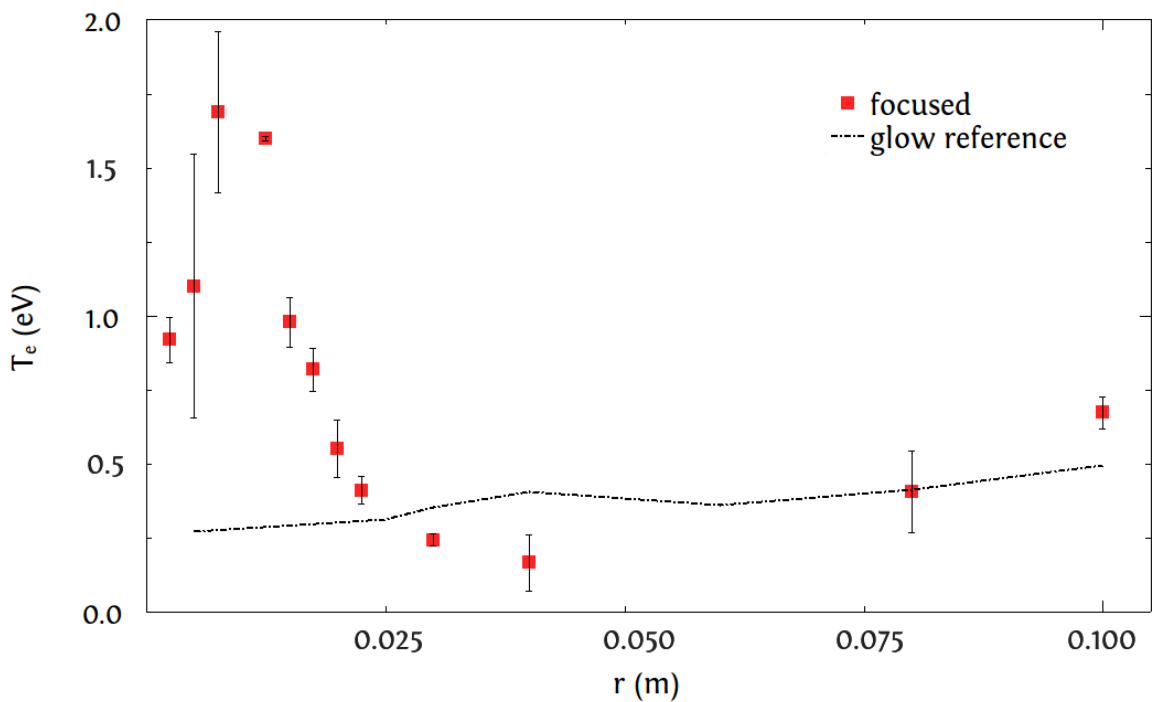

Figure 28. T_e spatial profile for a "focused" dipole plasma at $p = 4 \times 10^{-3} \, Torr$ and 0.25 kW of RF power, with "glow" reference.

With regards to the density (in figure 29), what we have is an agreement with the expectations from the pressure-power sweeping made with the Langmuir probe, as the

density in the "focused" configuration is at all times much higher than the density for the "glow" configuration.
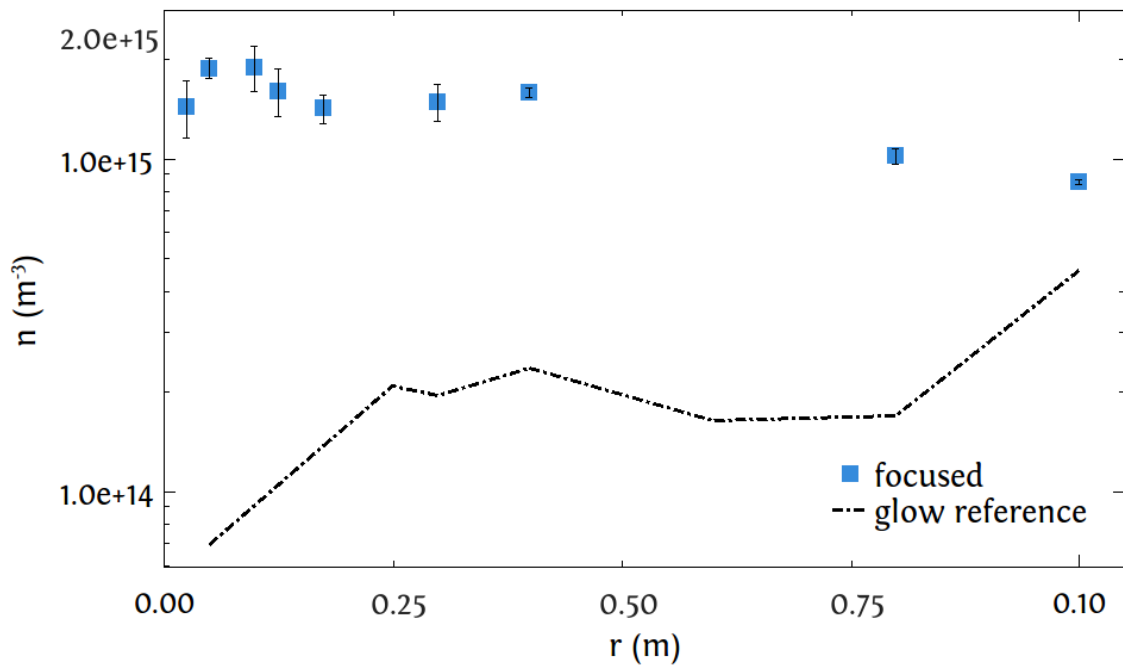

Figure 29. Density spatial profile for a "focused" dipole plasma at $p = 4 \times 10^{-3} Torr$ and 0.25 kW of RF power, with "glow" reference.

We see that characteristic electron temperatures for the "focused" plasma configuration are around 1 eV in the near field region, while in the far field region the electron temperature falls to the normal ("glow") values of around 0.5 eV and even lower as expected. And also we see that this plasma configuration yields densities one order of magnitude above the "glow" case, with typical densities of 10^{15} m^{-3}.

Figure 30 shows a zoom into the density spatial profile for the "focused" case, in order to better appreciate its features. The profile observed seems again to peak for a distance of 4 cm, but with a second and higher peak of $2 \times 10^{15} m^{-3}$ at the same distance range at which the electron temperature peaks. This is indicating that confinement of higher energy charged

particles is taking place in this region mainly, which is not the closest one to the magnet's surface. This is expected, since very close from the magnet the dipole approximation might not hold very faithful.
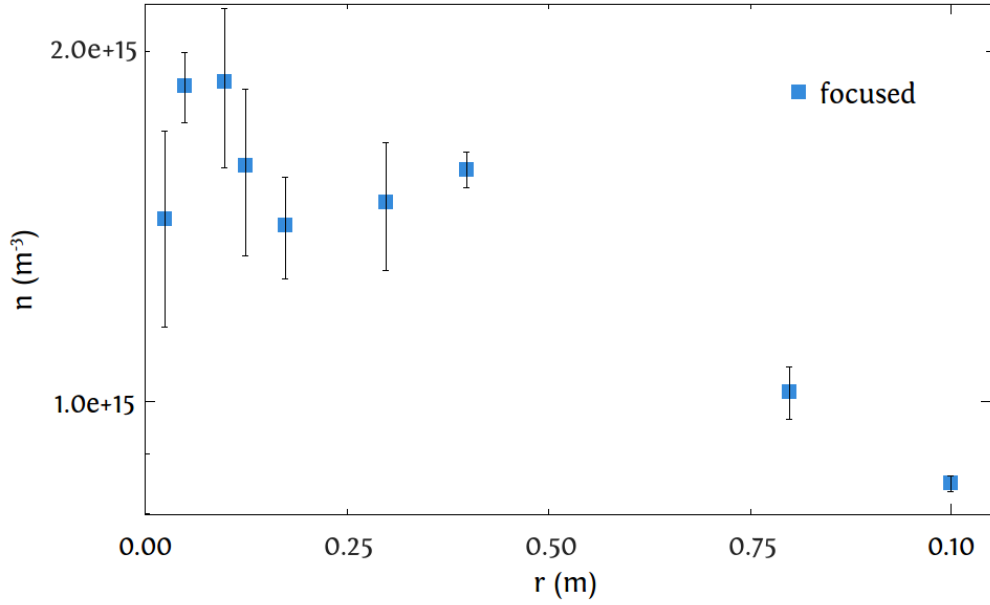

Figure 30. Density spatial profile for a "focused" dipole plasma at $p = 4 \times 10^{-3} Torr$ and 0.25 kW of RF power. Close up.

Having obtained the electron temperature and density profiles in space, it was possible to build a profile of the ionization ratio as well, according to Saha's equation that allows to relate the ionization ratio to the temperature and density. In this case, we use Saha's equation that is pertinent to our case with Helium used as filling gas,

$$\frac{n_i}{n_n} = \frac{2z_{II}}{nz_I} \left(\frac{2\pi m_e k T_e}{h^2} \right)^{3/2} e^{-X/kT} \tag{33}$$

where z stand for the weighted averages of neutral atoms in each energy stage, and X is the ionization energy from the ground state, which is 24.6 eV in the case of Helium. Because

almost all neutral atoms can be assumed to be in the ground state, and given the very high second ionization energy for helium of 54.4 eV, we can approximate $z_{II}/z_I \approx 1$.

Figure 31 shows the ionization ratio space profile obtained in this way.

Again we obtain a profile that peaks towards the surface of the magnet, before dropping right in front of it. The ionization ratio in this case reaches a significant peak at 0.5 cm from the magnet's surface, where an estimate of 1 out of 200 neutrals has become ionized. Around it, the ionization rate falls quickly an order of magnitude in either direction (closer or further from the magnet's surface). Yet further from the magnet (outside of the domain of figure 31), the ionization rate falls to levels in which no ionization is noticeable. In figure 31, the ionization is still significant until 2 cm away from the magnet, in which the neutrals density is millions of times higher than the ion density, and moving further away from there on makes the difference even higher.
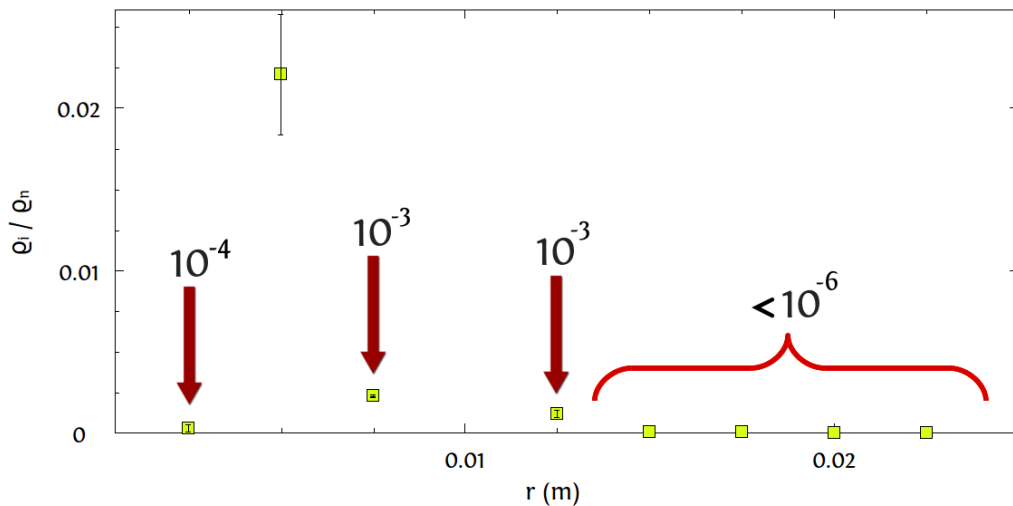

Figure 31. Ionization ratio spatial profile for a dipole plasma, at
$p=4\times10^{-3} Torr$ and 0.25 kW of RF power.

This is the final step to estimating whether we have been successful at fulfilling our objectives of building an experimental device for magnetospheric confinement of weakly-ionized ECH-generated plasma.

Chapter 4
Conclusions and Proposed Work

The present work has achieved the generation of an ECH plasma in a dipole field with a new experimental device and has explored the plasma's electron temperature and density profiles for different plasma configurations, as well as the ionization ratio for a plasma configuration of interest in which a central focused dipole plasma structure forms around a permanent magnet. The effects of the gas filling pressure and RF power used for the generation of plasma were examined under the light of Langmuir probe measurements and comparisons could be drawn between them.

Electron temperature and plasma density spatial profiles that peak towards the center, reaching Te ~ 2 eV and densities of $2 \times 10^{15} m^{-3}$ have seemed to be in agreement with Hasegawa's observations [1] on inward diffusion towards the center in a dipole plasma confinement approach, where plasma perpendicular temperature increases in proportion to B for the conservation of the first adiabatic invariant.

It was possible to determine a range of plasma structures and their dependency on filling pressure and RF power. A pressure-power phase-space was determined for the reproducibility of the plasma structures that rise at each combination of these parameters. This phase-space was used both as a guide to reproduce the conditions for each plasma configuration observed, and also as a diagnosis on itself.

The ionization ratio was found to reach a maximum of 2×10^{-2}, which provides for a wide range of scenarios to relate with astronomical plasmas and space weather, which is seeing many interesting applications these days including safety here on Earth [12].

Issues of wave accessibility have been discussed in cases in which ECH wave penetration was deemed choked by a too high density. Overall, the design, construction and generation of plasma in this new device has proven to serve the purpose of eased experimentation and study of plasma in a low-ionized regime, by using a neodymium permanent magnet as the source of the confining magnetic field.

Future work is proposed be carried out for magnetic field measurements as the experiment is conducted, and studies to determine the axisymmetry of the plasma configurations possible to realize in this new device. Most interestingly shall be the implementation of an electric field to drive a flow of plasma and allow for studies on accretion disks. The flexibility of the device would allow as well for the easy adaptation of different sources of magnetic field, such as the replacement of the permanent magnet for an array of coils through which current can be circulated.

56

Acknowledgments

The author would like to extend his heartfelt appreciation to all members of the Yoshida-Furukawa laboratory at the Department of Advanced Energy of the University of Tokyo, for their open-arms welcoming into their group and all the support and instruction that they provided in the course of these two years.

Especially to Professor Zensho Yoshida, for his valuable patience and scientific as well as academic guidance, always making every effort for this research to go unimpeded and for making a foreigner feel at home, both in Japan and the realms of plasma physics. The author feels indebted as well to Dr. Haruhiko Saitoh for his extraordinary and kind assistance, advice and support, with which it was possible for this study to reach its shore. Deep gratitude goes for Professor Masaru Furukawa and Mr. Junji Morikawa for their discussions and orientation provided at all times in the course of the Master's degree. The author also thanks his seniors Dr. Yoshihisa Yano and Mr. Yohei Kawazura for their availability at sharing of experience and know-how, as well as for their recommendations.

The author thanks the Ministry of Education, Culture, Sports, Science and Technology of Japan for the financial assistance of this research through the Monbukagakusho scholarship.

The author appreciates the talks on space weather held with Professor Ryuho Kataoka at Tokyo Institute of Technology, which provided further motivation into the study.

This work was made possible thanks to the continuous support beyond borders from Ximena Ruiz and Emilio Vogel and family.

Bibliography

[1] Hasegawa A. (1987) A dipole fusion reactor. *Comments on Plasma Physics and Controlled Fusion,* **11** 147.

[2] Mahajan S.M. and Yoshida Z. (1998) Double curl Beltrami flow: diamagnetic structures. *Physics Review Letters,* **81** 4863–4866.

[3] Hasegawa A. (2005) Motion of a charged particle and plasma equilibrium in a dipole magnetic field. *Physica Scripta,* **2005** T116.

[4] Kesner J., et al. (1998) The dipole fusion confinement concept. (Technical Report).

[5] Goto T., et al. (2006) Plasma production by electron cyclotron heating on the internal coil device Mini-RT. *Japanese Journal of Applied Physics,* **45**.

[6] Mizumaki S., et al. (2006) Development of the magnetically floating superconducting dipole in the RT-1 plasma device. *IEEE Transactions on Applied Superconductivity* **16**, 2.

[7] Krishan V. and Yoshida Z. (2006) Equilibrium structures in partially-ionized rotating plasmas within Hall MHD. *Physics of Plasmas,* **13** 092303.

[8] Krishan V. and Yoshida Z. (2009) Kolmogorov dissipation scales in weakly ionized plasmas. *Monthly Notices of the Royal Astronomical Society,* **395** 4.

[9] Saitoh H., et al. (2011) Formation of high-β plasma and stable confinement of toroidal electron plasma in Ring Trap 1. *Physics of Plasmas*, **18** 056102 .

[10] Saitoh H., et al. (2011) High-β plasma formation and observation of peaked density profile in RT-1. *Nuclear Fusion*, **51** 6.

[11] Kondoh S. and Yoshida Z. (1996) Toroidal magnetic confinement of non-neutral plasma. *Nuclear Instruments and Methods in Physics Research A*, **382** .

[12] Kataoka R., et al. (2011) Japanese challenge to predict the aviation radiation dose from solar energetic particles. *Space Weather*, in press.

[13] Witalis E. A. (1987) Hall effect magnetohydrodynamic (HMHD) plasma theory with applications. *Physica Scripta*, **35**.

[14] Balbus S. and Hawley J. F. (1998) Instability, turbulence, and enhanced transport in accretion disks. *Review of Modern Physics*, **70** 1.

[15] Nakashima C. and Yoshida Z. (1998) Application of RF electric field to a charged-particle trap in toroidal geometry. *Nuclear Instruments and Methods in Physics Research A*, **428**.

[16] Boxer A. C., et al. (2010) Turbulent inward pinch of plasma confined by a levitated dipole magnet. *Nature*, **6**.

[17] Furukawa M., et al. (2006) WKB analysis of axisymmetric magneto-rotational instability in a thin accretion disk. *Plasma and Fusion Research: Rapid Communications*, **1** 001.

[18] Furukawa M., et al. (2007) MHD stability in flowing plasmas: connection between fusion plasmas and astrophysics research. *Plasma and Fusion Research: Regular Articles*, **2** 016.

[19] Bernstein I. (1958) Waves in a plasma in a magnetic field. *Physical Review*, **109** 1.

[20] Yoshida Z., et al. (2007) RT-1 project: magnetosphere-like plasma experiment. *Transactions of Fusion Science and Technology*, **51**.

[21] Yoshida Z., et al. (2006) First plasma in the RT-1 device. *Plasma and Fusion Research: Rapid Communications*, **1** 008.

[22] Tosaka T., et al. (2006) Development of persistent-current mode HTS coil for the RT-1 plasma device. *IEEE Transactions on Applied Superconductivity*, **16** 2.

[23] Ogawa Y., et al. (2006) Application of high-temperature superconducting coil for internal ring devices. *Fusion Engineering and Design*, **81**.

[24] Shiraishi J., et al. (2006) A new-type equilibrium of flowing plasma dominated by the Hall effect. *Plasma and Fusion Research: Regular Articles*, **1** 050.

[25] Tosaka T., et al. (2007) First experiment on levitation and plasma with HTS magnet in the RT-1 plasma device. *IEEE Transactions on Applied Superconductivity*, **17** 2.

[26] Saitoh H., et al. (2007) Long-lived pure electron plasma in Ring Trap-1. *Plasma and Fusion Research: Rapid Communications*, **2** 045.

[27] Watanabe S., et al. (2008) Modification of probe characteristics in a supersonic plasma flow. *Plasma and Fusion Research: Letters*, **3** 019.

[28] Wesson J. (1987) Tokamaks. *Oxford University Press*, 3rd Edition, USA.

[29] Freidberg J. (2008) Plasma physics and fusion energy. *Cambridge University Press*, 1st Edition, New York.

[30] Chen F. F. (1965) Electric probes (from Plasma Diagnostic Techniques, edited by Hutchinson I. H.). *Academic Press*, New York.

[31] Hershkowitz N. (1989) How Langmuir probes work (from Plasma Diagnostics, Discharge Parameters and Chemistry, edited by Auciello O. and Flamm D. L.). *Academic Press*, London.

Publications and Conferences

1. Publications

"Formation of high-β plasma and stable confinement of toroidal electron plasma in RT-1" H. Saitoh, Z. Yoshida, J. Morikawa, M. Furukawa, Y. Yano, Y. Kawai, M. Kobayashi, G. Vogel, and H. Mikami, Physics of Plasmas 18, 056102 (April 2011).

"High-Beta Plasma Confinement and Inward Particle Diffusion in the Magnetospheric Device RT-1" (contributed paper) H. Saitoh, Z. Yoshida, J. Morikawa, Y. Yano, T. Mizushima, Y. Ogawa, M. Furukawa, K. Harima, Y. Kawazura, K. Tadachi, S. Emoto, M. Kobayashi, T. Sugiura, and G. Vogel, 23rd IAEA Fusion Energy Conference, Daejon, Korea (October 2010).

2. Conferences

"Hall MHD in a Magnetospheric, Weakly Ionized Plasma Device" (talk + poster session), G. Vogel 14th JAEA Plasma Workshop for Young Scientists, 7-9 March 2011, Naka, Japan.

"Formation of High-Beta Plasma and Stable Confinement of Toroidal Electron Plasma in RT-1" H. Saitoh, Z. Yoshida, J. Morikawa, M. Furukawa, Y. Yano, Y. Kawai, M. Kobayashi, G.Vogel, and H. Mikami 52nd Annual Meeting of the APS Division of Plasma Physics, 8-12 November 2010, Chicago, USA.